Pseudospectral solution of linear evolution equations of second order in space and time on unstructured quadrilateral subdomain topologies

D. Kondaxakis, S. Tsangaris

Fluids Section, School of Mechanical Engineering, National Technical University of Athens, 9 Heroon Polytechniou Avenue, 15773 Zografou, Athens, Greece

Abstract

A multidomain Legendre pseudospectral method is developed for the solution of linear hyperbolic initial boundary value problems, with mixed boundary conditions, in general two-dimensional and axisymmetric geometries. A weak collocation spectral method is utilized for the spatial approximation of a generic wave evolution equation over multiple nonoverlapping subdomains. The system of ordinary differential equations that stems from the above procedure is integrated in time by implicit as well as explicit high order temporal approximation algorithms. The weak formalism of the influence matrix method is combined with the implicit approximation, so as to efficiently solve the coupled system of linear equations after the full discretization, while a novel technique for avoiding the amplification of roundoff error at high temporal resolution simulations with the implicit temporal integration methods, is also studied. An innovative method for the treatment of Dirichlet boundary conditions is proposed, in order to avoid the order reduction which usually arises with the utilization of the explicit time integrator. Furthermore, appropriate modifications are reported, for dealing with the pole singularity problem faced by the weak formulation of axisymmetric problems. Finally, numerical simulations of a variety of wave problems on curvilinear geometries and unstructured subdomain configurations are presented in order to assess the capabilities of the proposed methodology in handling efficiently general hyperbolic differential operators.
© 2004 Elsevier Inc. All rights reserved.

Keywords: Second-order hyperbolic equations; Pseudospectral method; Domain decomposition; Unstructured topology

E-mail address: kond@fluid.mech.ntua.gr.

1. Introduction

Spectral methods constitute a highly accurate family of numerical methodologies for solving boundary value, eigenvalue and time-dependent problems [1–3]. Their collaboration with domain decomposition algorithms has succeeded in extending their range of applicability in problems formulated over complicated geometric configurations while preserving their inherent exponential convergence properties. The desirable features of spectral methods, regarding the solution of wave evolution problems, are mainly the excellent dispersion and dissipation characteristics. This has lead to their effective utilization in different areas of computational physics where wave phenomena play a fundamental role, like compressible fluid dynamics, aeroacoustics, computational electromagnetics, elastodynamics, engineering seismology and many others.

In the present paper, we develop a combination of a weak Legendre pseudospectral domain decomposition method for the spatial approximation, along with implicit and explicit high order temporal integration algorithms, for the solution of general initial boundary value problems of second order in both space and time, with mixed boundary conditions (of Dirichlet, Neumann and Robin type, including absorbing boundary conditions as well), over two-dimensional and axisymmetric computational domains. The particular spatial discretization method results from a modified variational formulation of the differential problem, which leads to a discrete weak Legendre collocation approximation in multiple subdomains. This methodology has been successfully used in the treatment of linear elliptic boundary value problems [4,5], in the solution of simple wave equations with mixed boundary conditions over rectangular geometries [6], as well as for the simulation of acoustic and elastic wave equations over structured subdomain configurations [7,8] and recently in the solution of the incompressible Navier–Stokes equations over unstructured quadrilateral subdomain topologies in [9]. We provide a unified form of the method able to efficiently handle coordinate transformations, curvilinear solution domains and unstructured subdomain partitions, by successfully treating grid nodes which simultaneously belong to more than one subdomains and thus achieving time domain solutions of wave propagation problems over complex geometries. We utilize this method both for imposing Neumann and Robin boundary operators with enhanced accuracy and for naturally treating the equations that govern the interface unknowns, in a way which resembles the well-established finite element and spectral element algorithms but in a pure spectral collocation framework.

The system of ordinary differential equations which arises from the spatial discretization procedure is integrated in time using implicit temporal approximation schemes which belong to the family of Newmark time integrators, as well as a classical high resolution explicit Runge–Kutta–Nyström temporal discretization algorithm. A weak formulation of the influence matrix technique is utilized for the decoupling of the equations for the internal nodes from the ones governing the interface and some of the boundary unknowns, while a combination of direct methods is used for tackling effectively the linear algebraic system of discrete equations resulting from the approximation by the implicit temporal integration method. A novel technique for avoiding the uncontrollable increase of the roundoff error with the implicit method is investigated, while a very efficient method for surmounting the problem of order reduction, which typically occurs with the usage of Runge–Kutta type integrators, is also formulated in a way consistent with the nature of the spatial discretization method employed. Finally, we report the necessary modifications that have to take place for the successful treatment of the pole singularity encountered at axisymmetric formulations of initial boundary value problems, which differ in accordance to the type of method used for the time integration.

The present paper is organized as follows. Section 2 gives the mathematical formulation of the generic initial boundary value problem. In Section 3, the continuous and discrete forms of the spatial approximation method are presented. The temporal discretization methods utilized in this work, as well as some aspects of their implementation, are reported in Section 4. Finally, Section 5 is completely devoted to the numerical simulations of a plethora of wave evolution problems, starting with simple model problems in order to establish the convergence properties of the numerical methods and ending with more realistic and complicated solutions of general hyperbolic differential equations.

2. The initial boundary value problem

We consider a two-dimensional open and bounded domain $\Omega \subset \Re^2$ with a Lipschitz continuous boundary $\partial\Omega$, a time interval $I = (0, T) \subset \Re$ with $T > 0$, and set $\Omega_I = \Omega \times I$. The boundary $\partial\Omega$ can be decomposed into three open, bounded and mutually disjoint sets namely Γ_D, Γ_N and Γ_R such that $\bar{\Gamma}_D \cup \bar{\Gamma}_N \cup \bar{\Gamma}_R = \partial\Omega$, $\Gamma_D \cap \Gamma_N = \emptyset$, $\Gamma_N \cap \Gamma_R = \emptyset$ and $\Gamma_R \cap \Gamma_D = \emptyset$, where the overlying bar is used to indicate closed domains.

Let us introduce, at this point, some functional spaces that will prove to be very helpful in the subsequent presentation. Let X be a subset of $\Re^n$ ($n = 1$, 2 or 3) and Y be a linear topological space. By $[Y]^2$ we indicate the product space $Y \times Y$. We denote by $C^0(X)$ the space consisting of all functions $F: X \to Y$ defined on X, which are bounded and continuous with respect to the topology of Y. Then for $m = 1, 2, \ldots$ we define $C^m(X)$ to be the totality of functions which possess continuous and bounded partial derivatives of all orders less or equal than m, in X. Clearly, $C^\infty(X) = \bigcap_{m=1}^{\infty} C^m(X)$. When Y is a subset of $\Re^n$ it is assumed to be endowed with the usual metric topology. Finally, we use the customary notation $L^p(X)$, ($1 \leqslant p < \infty$) for the family of spaces of Lebesgue integrable functions over X, $L^\infty(X)$ for the set of essentially bounded functions and $H^m(X)$, $m = 0, 1, 2, \ldots$ for the Sobolev spaces of integer order.

We proceed by defining a linear spatial differential operator of the form:

$$L = -\sum_{i=1}^{2} \sum_{j=1}^{2} \frac{\partial}{\partial x_i}\left(a_{ij}\frac{\partial}{\partial x_j}\right) + \sum_{j=1}^{2} a_j\frac{\partial}{\partial x_j} + a_0 I_d,$$

where $\vec{x} = (x_1, x_2) = (x, y)$ is an element of $\Re^2$ and I_d is the identity operator. We assume that the coefficients $a_{ij}, a_j, a_0 : \Omega_I \to \Re$ belong to $C^\infty(\Omega_I)$. The above operator is said to satisfy the strictly elliptic hypothesis, if for every $\vec{x} \in \Omega$ and $t \in I$, positive constants λ_0 and μ_0 exist such that the following relation holds:

$$\mu_0 \sum_{j=1}^{2} \xi_j^2 \geqslant \sum_{i=1}^{2} \sum_{j=1}^{2} a_{ij}(\vec{x}, t)\xi_i\xi_j \geqslant \lambda_0 \sum_{j=1}^{2} \xi_j^2,$$

for every real vector $\vec{\xi} = (\xi_1, \xi_2)$. Moreover, we define a function $c : \Omega_I \to \Re$ such that $c \in C^\infty(\Omega_I)$, together with the following seven scalar fields $u_0, u_1 : \Omega \to \Re$, $g : \Gamma_D \times I \to \Re$, $h : \Gamma_N \times I \to \Re$ and $q, b_0, b_1 : \Gamma_R \times I \to \Re$. We demand that $b_0, b_1 \in C^\infty(\Gamma_R \times I)$ and $b_0 \geqslant 0 \ \forall(\vec{x}, t) \in \Gamma_R \times I$.

Suppose that we have the initial boundary value problem of finding a function $u = u(\vec{x}, t) : \Omega_I \to \Re$ that satisfies:

$$\left\|\begin{array}{ll} H[u] = \frac{\partial^2 u}{\partial t^2} + c\frac{\partial u}{\partial t} + L[u] = f & \text{on } \Omega_I, \\ u = u_0 & \text{on } \Omega \text{ for } t = 0, \\ \frac{\partial u}{\partial t} = u_1 & \text{on } \Omega \text{ for } t = 0, \\ u = g & \text{on } \Gamma_D \times I, \\ \frac{\partial u}{\partial n_L} = h & \text{on } \Gamma_N \times I, \\ \frac{\partial u}{\partial n_L} + b_0\frac{\partial u}{\partial t} + b_1 u = q & \text{on } \Gamma_R \times I, \end{array}\right. \tag{1}$$

with $\frac{\partial u}{\partial n_L} = \vec{D}_L[u] \cdot \vec{n} = \sum_{i=1}^{2}\sum_{j=1}^{2} a_{ij}\frac{\partial u}{\partial x_j}n_i$ the "transversal" (or "co-normal") derivative with respect to L, $\vec{n} = (n_1, n_2)$ the outward unit normal vector on $\partial\Omega$, and f a given real-valued function on Ω_I. Clearly, when Γ_R is not empty, the functions b_0 and b_1 cannot be simultaneously equal to zero on Γ_R for $t \in I$. Problem (1) is the strong formulation of a generic linear evolution partial differential equation of second order both in space and time, supplemented with proper initial and mixed boundary conditions of all types (Dirichlet, Neumann and Robin) so that the well-posedness of the total problem is ensured. The strictly elliptic nature of L leads us to conclude that H is a normal hyperbolic operator. For a complete mathematical analysis of such problems from a functional analytic point of view, the interested reader could consult [10]. The choice

of the initial wave field u_0 and of its first temporal derivative u_1 is certainly not arbitrary. A rigorous discussion on the countably infinite set of compatibility conditions that must be satisfied by the initial conditions, for the solution to be analytic everywhere in the space–time domain, is supplied in [11].

3. Spatial discretization method

In the following sections, we apply the method of lines in order to discretize the spatial differential operators while leaving the temporal ones continuous and so formulating a semi-discrete version of the initial boundary value problem. Towards this end, we utilize the weak Legendre collocation method, which is a member of the family of generalized Galerkin techniques, and has been successfully used in [9,12,13] to tackle diverse problems in mathematical physics. First, we state the variational formulation of the problem and then we proceed sequentially with the continuous and discrete versions of the spatial approximation method.

3.1. Continuous formulation

The variational formulation of problem (1) reads:

$$\left\| \begin{array}{l} u \in U = \{u(t) : I \to H^1(\Omega)|u = g \quad \text{on } \Gamma_{\mathrm{D}} \times I\}, \\ a(t; u, v) = b(t; v) \quad \forall v \in V = \{v \in H^1(\Omega)|v = 0 \text{ on } \Gamma_{\mathrm{D}}\}, \ t \in I, \end{array} \right. \tag{2}$$

where the above forms are given as:

$$a(t; u, v) = \int_\Omega \int \left(\frac{\partial^2 u}{\partial t^2} v + c \frac{\partial u}{\partial t} v + \sum_{i=1}^2 \sum_{j=1}^2 a_{ij} \frac{\partial u}{\partial x_j} \frac{\partial v}{\partial x_i} + \sum_{j=1}^2 a_j \frac{\partial u}{\partial x_j} v + a_0 uv \right) + \int_{\Gamma_{\mathrm{R}}} \left(b_0 \frac{\partial u}{\partial t} + b_1 u \right) v,$$

$$b(t; v) = \int_\Omega \int fv + \int_{\Gamma_{\mathrm{N}}} hv + \int_{\Gamma_{\mathrm{R}}} qv,$$

with $\frac{\partial^2 u}{\partial t^2}(t), \frac{\partial u}{\partial t}(t), f(t) : I \to L^2(\Omega), h(t) : I \to L^2(\Gamma_{\mathrm{N}}), q(t) : I \to L^2(\Gamma_{\mathrm{R}})$. We should add that here and in some parts of the following text, we do not indicate the integration measures in the integral forms for the sake of simplicity.

In the framework of a domain decomposition method, we subdivide the computational domain Ω, into open and bounded nonoverlapping quadrilateral subdomains Ω^m, $m \in M$, (M being a set of positive integers) in a generally unstructured way so as $\bar{\Omega} = \bigcup_{m \in M} \bar{\Omega}^m$, and $\Omega^k \cap \Omega^l = \emptyset$ for $k \neq l$. This subdivision is such that the closures of two neighboring subdomains are allowed to intersect only at a point or along an entire side and that the subdomain borders remain stationary for all times. We define the sets $\Gamma_{\mathrm{N}}^m = \partial \Omega^m \cap \Gamma_{\mathrm{N}}$ and $\Gamma_{\mathrm{R}}^m = \partial \Omega^m \cap \Gamma_{\mathrm{R}}$, so the functionals that appear in the variational formulation (2) obtain the following form:

$$\begin{aligned} a(t; u, v) = & \sum_{m \in M} \int_{\Omega^m} \int \left(\frac{\partial^2 u^m}{\partial t^2} v^m + c^m \frac{\partial u^m}{\partial t} v^m + \sum_{i=1}^2 \sum_{j=1}^2 a_{ij}^m \frac{\partial u^m}{\partial x_j} \frac{\partial v^m}{\partial x_i} + \sum_{j=1}^2 a_j^m \frac{\partial u^m}{\partial x_j} v^m + a_0^m u^m v^m \right) \\ & + \sum_{m \in M} \int_{\Gamma_{\mathrm{R}}^m} \left(b_0^m \frac{\partial u^m}{\partial t} + b_1^m u^m \right) v^m, \end{aligned}$$

$$b(t; v) = \sum_{m \in M} \left\{ \int_{\Omega^m} \int f^m v^m + \int_{\Gamma_{\mathrm{N}}^m} h^m v^m + \int_{\Gamma_{\mathrm{R}}^m} q^m v^m \right\}.$$

By the superscript m on functions we indicate their restriction in the subdomain Ω^m. The same superscript on differential operators is used to denote the restriction of their action on the subspace of functions defined on Ω^m, as well as the replacement of the coefficient functions by their restrictions in the specific subdomain.

Assuming that:

$$u \in \hat{U} = \{u(t) : I \to H^2(\Omega) | u = g \text{ on } \Gamma_D \times I\},$$

we see that the bilinear form a can be transformed into:

$$a(t; u, v) = \sum_{m \in M} \left\{ \int_{\Omega^m} \int \left(\frac{\partial^2 u^m}{\partial t^2} + c^m \frac{\partial u^m}{\partial t} + L^m[u^m] \right) v^m + \oint_{\partial \Omega^m} \left(\vec{D}_L^m[u^m] \cdot \vec{n}^m \right) v^m \right\}$$
$$+ \sum_{m \in M} \int_{\Gamma_R^m} \left(b_0^m \frac{\partial u^m}{\partial t} + b_1^m u^m \right) v^m.$$

Clearly, for the above form to be correctly defined, we may only require:

$$v \in \hat{V} = \{v \in L^2(\Omega) | v = 0 \text{ on } \Gamma_D\}.$$

In view of the fact that the subdomain topology is globally unstructured and that the boundaries $\partial \Omega^m$ are generally curvilinear, we assume that there exists a family of isomorphisms $\vec{F}^m$, $m \in M$, that map the reference square $\bar{D} = [-1, 1]^2$ onto each subdomain $\bar{\Omega}^m$, in such a way that the reference border ∂D is also mapped onto the subdomain one $\partial \Omega^m$. We set a typical element of $\bar{D}$ as the ordered pair of real numbers $\vec{r} = (r_1, r_2) = (r, s)$ and indicate any point in $\bar{\Omega}^m$ by $\vec{x}^m = (x_1^m, x_2^m) = (x^m, y^m)$. Using the proceeding notation, we can write:

$$\vec{F}^m : \bar{D} \to \bar{\Omega}^m, \quad \vec{F}^m \in [C^2(\bar{D})]^2 : \vec{x}^m = \vec{F}^m(\vec{r}), \quad m \in M.$$

The Jacobian of the coordinate transformation, which is defined as $J^m = \det(\partial x_i^m / \partial r_j^m)$, $i, j = 1, 2$, $m \in M$, differs from zero at every point in each subdomain and since it never changes sign inside the same subdomain, it can be used in order to characterize the orientation of the boundaries $\partial \Omega^m$.

Let us set the four sides of the subdomain $\bar{\Omega}^m$ as $\Gamma^{m,p}$, $p = 1, \ldots, 4$, so that $\bigcup_{p=1}^4 \bar{\Gamma}^{m,p} = \partial \Omega^m$. Accordingly, we may define the four sides of the parent element $\bar{D}$ as S^p, $p = 1, \ldots, 4$, with $\bigcup_{p=1}^4 \bar{S}^p = \partial D$. As we have already stated, the coordinate transformation operator maps each of the S^p onto each of the $\Gamma^{m,p}$, so that we can symbolically write $\Gamma^{m,p} = \vec{F}^m(S^p)$, $m \in M$, $p = 1, \ldots, 4$. Finally, let P_N^m and P_R^m be the index sets:

$$P_N^m = \left\{ p \,|\, 1 \leqslant p \leqslant 4, \Gamma^{m,p} \subseteq \Gamma_N^m, \Gamma^{m,p} = \vec{F}^m(S^p), m \in M \right\},$$

$$P_R^m = \left\{ p \,|\, 1 \leqslant p \leqslant 4, \Gamma^{m,p} \subseteq \Gamma_R^m, \Gamma^{m,p} = \vec{F}^m(S^p), m \in M \right\}.$$

After all of these, the modified variational formulation of the generalized initial boundary value problem (1), is:

$$\left\|\begin{array}{l} u \in \hat{U}, \\ a(t; u, v) = b(t; v) \quad \forall v \in \hat{V}, \ t \in I, \end{array}\right. \tag{3}$$

where:

$$a(t; u, v) = \sum_{m \in M} \int_{s=-1}^{1} \int_{r=-1}^{1} \left(\frac{\partial^2 u^m}{\partial t^2} + c^m \frac{\partial u^m}{\partial t} + L^m[u^m] \right) v^m |J^m| \, dr \, ds$$

$$+ \sum_{m \in M} \sum_{p=1}^{4} \int_{\substack{\zeta^p = -1 \\ S^p}}^{1} \left(\vec{D}_L^m[u^m] \cdot \vec{N}^{m,p} \right) v^m d\zeta^p + \sum_{m \in M} \sum_{p \in P_R^m} \int_{\substack{\zeta^p = -1 \\ S^p}}^{1} \left(b_0^m \frac{\partial u^m}{\partial t} + b_1^m u^m \right) v^m \left\| \vec{N}^{m,p} \right\| d\zeta^p,$$

$$b(t; v) = \sum_{m \in M} \int_{s=-1}^{1} \int_{r=-1}^{1} f^m v^m |J^m| \, dr \, ds + \sum_{m \in M} \sum_{p \in P_N^m} \int_{\substack{\zeta^p = -1 \\ S^p}}^{1} h^m v^m \left\| \vec{N}^{m,p} \right\| d\zeta^p$$

$$+ \sum_{m \in M} \sum_{p \in P_R^m} \int_{\substack{\zeta^p = -1 \\ S^p}}^{1} q^m v^m \left\| \vec{N}^{m,p} \right\| d\zeta^p.$$

The dummy variable ζ^p and the integration measures $d\zeta^p$ are determined in accordance with the sets S^p over which the line integrals are defined. The specific form of the vectors $\vec{N}^{m,p}$ is given in [9], while the symbol $\| \ \|$ indicates the norm function which defines the usual metric topology of $\Re^2$.

3.2. Discrete formulation

In the present subsection, we proceed with the spatially discretized form of the modified continuous variational formulation of the generic initial boundary value problem. Given a positive integer N, we define the space $P_N(\bar{D})$ as the totality of continuous functions up to the boundary, which are real-valued algebraic polynomials of degree less or equal than N in each independent spatial variable. Obviously, we have $P_N(\bar{D}) \subset C^0(\bar{D})$. The approximants (or interpolants as we later state) u_N^m of the restrictions u^m of u, in each subdomain, belong to $P_N(\bar{D})$.

Next, we introduce a set of distinct nodes that covers $\bar{D}$. We consider the integer vector index $\vec{j} = (j_1, j_2)$, $0 \leqslant j_1, j_2 \leqslant N$ and define the set:

$$J = \left\{ \vec{j} = (j_1, j_2) \mid 0 \leqslant j_1, j_2 \leqslant N, \vec{r}_{\vec{j}} = (r_{j_1}, s_{j_2}) \in \bar{D} \right\}.$$

The collocation mesh on $\bar{D}$ is expressed as the set of points $\{ \vec{r}_{\vec{j}} \}_{\vec{j} \in J}$. In a similar way, we define the boundary index sets to be:

$$J_b^p = \left\{ \vec{j} = (j_1, j_2) \mid 0 \leqslant j_1, j_2 \leqslant N, \vec{r}_{\vec{j}} = (r_{j_1}, s_{j_2}) \in \bar{S}^p \right\}, \quad p = 1, \ldots, 4.$$

The grids $\vec{x}_{\vec{j}}^m = (x_{j_1}^m, y_{j_2}^m) = \vec{F}^m (\vec{r}_{\vec{j}}) \in \bar{\Omega}^m, \vec{j} \in J$, that cover each subdomain are calculated by applying the coordinate transformation operators on the reference mesh. Next, let us introduce a global numbering system of nodes by assigning a different scalar index to each grid point and define the set:

$$J^G = \left\{ l \mid \vec{x}_l = (x_l, y_l) \in \bar{\Omega} \right\},$$

where l is a positive integer. The whole pseudospectral grid over the computational domain may now be written as $\{ \vec{x}_l \}_{l \in J^G}$. In a similar manner, we are able to denote the subsets of indices of the nodes, in the global numbering system, on which we impose Dirichlet, Neumann or Robin boundary conditions as $J_{b,D}^G \subset J^G, J_{b,N}^G \subset J^G$ and $J_{b,R}^G \subset J^G$, respectively. The existence of two numbering systems mandates the introduction of a non-invertible operator $G : M \times J \to J^G$, which determines the correlations between the subdomains, the local and the global indices.

For a detailed definition of the local $\{ \phi^{\vec{j}}(\vec{r}) \}_{\vec{j} \in J}$ and global $\{ v^l(\vec{x}) \}_{l \in J^G}$ Lagrange basis, we refer to previously published work (see [9]). By using the local basis functions we are in the position to express the interpolants u_N^m as:

$$u_N^m(\vec{r},t) = \sum_{\vec{j} \in J} \langle u_N^m \rangle_{\vec{j}}(t) \phi^{\vec{j}}\left(\vec{r}\right),$$

where $\langle u_N^m \rangle_{\vec{j}}(t) = u_N^m(\vec{r}_{\vec{j}},t) = u_N^m(r_{j_1},s_{j_2},t)$ for all $t \in I$. In order to accomplish a high order representation of the geometry, we employ the isoparametric technique already used in [14], which allows us to define the geometric variables by the same spatial interpolation rules as the unknown function of the differential equation, in the framework of a fully conformal discrete approximation.

Before proceeding with the discretization of the modified variational formulation, we need to fix a family of weights $w_j > 0$, $0 \leqslant j \leqslant N$, and set the bilinear form:

$$(f_a, f_b)_N = \sum_{\vec{j} \in J} \langle f_a \rangle_{\vec{j}} \langle f_b \rangle_{\vec{j}} \omega_{\vec{j}},$$

where $\omega_{\vec{j}} = w_{j_1} w_{j_2}$, while $f_a(t), f_b(t) : I \to C^0(\bar{D})$ are arbitrary functions with $\langle f_a \rangle_{\vec{j}} = f_a(r_{j_1},s_{j_2},t)$, $\langle f_b \rangle_{\vec{j}} = f_b(r_{j_1},s_{j_2},t)$ for every $t \in I$. By determining the $\vec{r}_{\vec{j}}$ and $\omega_{\vec{j}}$, $j \in J$, as the knots and weights, respectively, of quadrature formulas of Gaussian type, we can approximate the double integral $\int_{s=-1}^{1} \int_{r=-1}^{1} f_a f_b \, dr \, ds$ by $(f_a, f_b)_N$, with maximum precision. Similarly, the line integrals may be expressed as:

$$\int_{\zeta^p = -1}^{1} f_a \, d\zeta^p = \sum_{\vec{j} \in J_b^p} \langle f_a \rangle_{\vec{j}} \omega_{\vec{j}}^p,$$

where $\omega_{\vec{j}}^p = w_{j_1}$ or w_{j_2} in accordance with the integration domain S^p.

The subscript N on functions indicates their polynomial interpolant, while the same subscript at the expressions of the differential forms denotes the approximations to these operators obtained by replacing the exact derivatives by collocation ones. For notational convenience, we use $\langle f_D \rangle_{\vec{i}} = f_D(r_{i_1},s_{i_2},t)$, $i \in J$, and $\langle f_\Omega \rangle_l = f_\Omega(x_l,y_l,t)$, $l \in J^G$, for functions that are correspondingly defined on $\bar{D}$ and $\bar{\Omega}$ for all $t \in I$. Furthermore, we define a set of subdomain indices as $M^l = \{m \in M | \vec{x}_l \in \bar{\Omega}^m, l \in J^G\} \subseteq M$ and also assume that the indices $l \in J^G$ and $\vec{j}_m \in J$ are related through $l = G(m, \vec{j}_m)$, with $m \in M^l$. Finally, the discrete form of the modified variational formulation (3) may be given as:

$$\left\| \begin{array}{l} u_N \in \hat{U}_N, \\ a_N(t; u_N, v_N^l) = b_N(t; v_N^l) \quad \forall v_N^l \in \hat{V}_N, \ t \in I, \end{array} \right. \tag{4}$$

where we have indicated the spaces of trial and test functions by:

$$\hat{U}_N = \left\{ u_N(t) : I \to C^0(\bar{\Omega}) \,|\, u_N^m(t) : I \to P_N(\bar{D}), m \in M, \langle u_N \rangle_l(t) = \langle g_N \rangle_l(t) \text{ for } l \in J_{b,D}^G, t \in I \right\},$$

$$\hat{V}_N = \left\{ v_N^l \in C^0(\bar{\Omega}), l \in J^G \,|\, v_N^{l,m} \in P_N(\bar{D}), m \in M^l \text{ and } v_N^l = 0 \text{ in } \bar{\Omega} \text{ for } l \in J_{b,D}^G \right\}.$$

The linear functionals that are included in the above discretization, are given by the following formulas:

$$\begin{aligned}
a_N(t; u_N, v_N^l) &= \sum_{m \in M^l} \sum_{\vec{i} \in J} \left(\frac{d^2 \langle u_N^m \rangle_{\vec{i}}}{dt^2} + \langle c_N^m \rangle_{\vec{i}} \frac{d\langle u_N^m \rangle_{\vec{i}}}{dt} + \langle L_N^m[u_N^m] \rangle_{\vec{i}} \right) \left\langle \phi^{\vec{j}_m} \right\rangle_{\vec{i}} \langle |J_N^m| \rangle_{\vec{i}} \omega_{\vec{i}} \\
&\quad + \sum_{m \in M^l} \sum_{p=1}^{4} \sum_{\vec{i} \in J_b^p} \left\langle \vec{D}_{L_N}^m[u_N^m] \cdot \vec{N}^{m,p} \right\rangle_{\vec{i}} \left\langle \phi^{\vec{j}_m} \right\rangle_{\vec{i}} \omega_{\vec{i}}^p \\
&\quad + \sum_{m \in M^l} \sum_{p \in P_R^m} \sum_{\vec{i} \in J_b^p} \left(\langle b_{0,N}^m \rangle_{\vec{i}} \frac{d\langle u_N^m \rangle_{\vec{i}}}{dt} + \langle b_{1,N}^m \rangle_{\vec{i}} \langle u_N^m \rangle_{\vec{i}} \right) \left\langle \left\| \vec{N}^{m,p} \right\| \right\rangle_{\vec{i}} \left\langle \phi^{\vec{j}_m} \right\rangle_{\vec{i}} \omega_{\vec{i}}^p,
\end{aligned}$$

$$b_N(t; v_N^l) = \sum_{m \in M^l} \sum_{\vec{i} \in J} \langle f_N^m \rangle_{\vec{i}} \left\langle \phi^{\vec{j}_m} \right\rangle_{\vec{i}} \langle |J_N^m| \rangle_{\vec{i}} \omega_{\vec{i}}$$
$$+ \sum_{m \in M^l} \sum_{p \in P_N^m} \sum_{\vec{i} \in J_b^p} \langle h_N^m \rangle_{\vec{i}} \left\langle \left\| \vec{N}^{m,p} \right\| \right\rangle_{\vec{i}} \left\langle \phi^{\vec{j}_m} \right\rangle_{\vec{i}} \omega_{\vec{i}}^p$$
$$+ \sum_{m \in M^l} \sum_{p \in P_R^m} \sum_{\vec{i} \in J_b^p} \langle q_N^m \rangle_{\vec{i}} \left\langle \left\| \vec{N}^{m,p} \right\| \right\rangle_{\vec{i}} \left\langle \phi^{\vec{j}_m} \right\rangle_{\vec{i}} \omega_{\vec{i}}^p.$$

We have chosen to apply the pseudospectral method in the framework of a Legendre approximation (see [1–3]) in order to maintain maximum precision in the discrete evaluation of the integral forms. This means that the knots and weights previously defined, correspond to the Legendre–Gauss–Lobatto quadrature formula. To be more precise, if we use the variable ξ to denote either r or s, then we define $\xi_0 = -1$, $\xi_N = 1$ and $\{\xi_j\}_{j=1}^{N-1}$ to be the zeroes of $dP_N^L/d\xi$, where $P_N^L(\xi)$ stands for the Legendre polynomial of degree N. Accordingly, the family of weights is fixed as $w_j = \frac{2}{N(N+1)} \frac{1}{[P_N^L(\xi_j)]^2}$ for all $j = 0, \ldots, N$. Finally, the Lagrange basis functions are defined over the Gauss–Lobatto points, while the discrete approximation of the differential operators is generated by using Legendre pseudospectral derivatives.

In this section, we described the spatially discretized version of the variational formulation of a generic initial boundary value problem of second order. The ellipticity of the spatial operator allowed us to utilize the weak Legendre collocation method for deriving the discrete set of equations. The main differences between the weak and the strong formalisms occur at the way the Neumann and Robin boundary conditions are enforced, as well as at the setting of the conditions for the nodes that lie on the interface between neighboring subdomains. Previous studies both on elliptic and on hyperbolic problems (see [4–6]), have shown that the weak imposition of Neumann and Robin boundary operators enjoys higher accuracy and prevents the undesirable onset of numerically induced oscillations due to inadequate evaluation of the transversal derivatives near the boundary in contradiction with the strong (pointwise) formulation. Before ending this section, let us mention that the type of interface conditions which stem from the weak formalism is clearer and undoubtedly outclasses the traditional C^1 enforcement used with the classical pseudospectral formulation, especially at points where more than two subdomains meet which typically occur at unstructured subdomain partitions.

4. Temporal discretization methods

Subsequently, we proceed by discretizing the temporal differential operators and thus ending with the fully discrete form of the linear initial boundary value problem. In this process, we utilize both implicit as well as explicit self-starting time integration methods. Let us introduce some notational conventions which will greatly facilitate the following presentation. We are in the position to define an index set of positive integers as $J_t = \{n \in \mathrm{N} \,|\, 0 \leqslant n < K, K \in \mathrm{N} \backslash \{0\}\}$, where K stands for any natural number different from 0. The constant time step interval can be introduced as the ratio $\Delta t = T/K$. We may set a uniform grid on the closed time interval as the set of distinct points $\{t^n \in \bar{I} \,|\, t^n = n\Delta t, n \in J_t \cup \{K\}\}$. For simplicity, throughout this section we use, $\langle f_D \rangle_{\vec{i}}^n = f_D(r_{i_1}, s_{i_2}, t^n)$, $i \in J$, and $\langle f_\Omega \rangle_l^n = f_\Omega(x_l, y_l, t^n)$, $l \in J^G$, with $n \in J_t \cup \{K\}$ for functions that (for all $t \in \bar{I}$) are defined on $\bar{D}$ and $\bar{\Omega}$, respectively, and where the superscripts are used to denote discrete time levels.

4.1. Newmark family of time integration methods

In this subsection, we choose the Newmark family of schemes in order to discretize the problem in time (see [15,16]). These methods are characterized by a set of two parameters $\beta \in (0, \frac{1}{2}]$ and $\gamma \in [\frac{1}{2}, 1]$, which determine the accuracy and stability properties of the different schemes. We consider only implicit methods in this work, so we exclude the zero value from the domain of definition of β. A commonly used choice of

parameters is $(\beta, \gamma) = (\frac{1}{4}, \frac{1}{2})$, that leads to the second-order accurate unconditionally stable average acceleration scheme, and which is certainly the one we utilize at the section of the numerical simulations. Next, we introduce two functions, namely $u^{(1)}$ and $u^{(2)}$, which serve as approximations of $\partial u/\partial t$ and $\partial^2 u/\partial t^2$, respectively, and will prove to be of paramount importance in the subsequent discussion. We present the method in a predictor–corrector form since it offers obvious advantages from an implementational point of view (the overlying tildes are used to denote intermediate auxiliary dependent variables):

- Prediction step:
  At each time step and for each node that does not belong to the Dirichlet boundary, compute:
  $$\left\langle \tilde{u}_N^{(1)} \right\rangle_l^{n+1} = \left\langle u_N^{(1)} \right\rangle_l^n + \Delta t(1-\gamma)\left\langle u_N^{(2)} \right\rangle_l^n,$$

  $$\langle \tilde{u}_N \rangle_l^{n+1} = \langle u_N \rangle_l^n + \Delta t \left\langle u_N^{(1)} \right\rangle_l^n + \frac{\Delta t^2}{2}(1-2\beta)\left\langle u_N^{(2)} \right\rangle_l^n,$$

  for $l \in J^G \setminus J_{b,D}^G$ and $n \in J_t$.

- Solution step:
  Next, solve the following discrete linear elliptic boundary value problem:
  $$\left\| \begin{array}{l} u_N \in \hat{U}_N^{n+1}, \\ a_N^e(u_N, v_N^l) = b_N^e(v_N^l) \quad \forall v_N^l \in \hat{V}_N, \end{array} \right.$$

  where:
  $$\hat{U}_N^{n+1} = \left\{ u_N \in C^0(\bar{\Omega}), t = t^{n+1} \,|\, u_N^m \in P_N(\bar{D}), t = t^{n+1}, m \in M, \langle u_N \rangle_l^{n+1} = \langle g_N \rangle_l^{n+1} \text{ for } l \in J_{b,D}^G \right\},$$

  and:
  $$\begin{aligned}
  a_N^e(u_N, v_N^l) &= \sum_{m \in M^l} \sum_{\vec{i} \in J} \left(\langle L_N^m[u_N^m] \rangle_{\vec{i}}^{n+1} + \frac{1}{\beta \Delta t^2} \langle u_N^m \rangle_{\vec{i}}^{n+1} + \frac{\gamma}{\beta \Delta t} \langle c_N^m \rangle_{\vec{i}}^{n+1} \langle u_N^m \rangle_{\vec{i}}^{n+1} \right) \left\langle \phi^{\vec{j}_m} \right\rangle_{\vec{i}} \langle |J_N^m| \rangle_{\vec{i}} \omega_{\vec{i}} \\
  &\quad + \sum_{m \in M^l} \sum_{p=1}^4 \sum_{\vec{i} \in J_b^p} \left\langle \vec{D}_{L_N}^m[u_N^m] \cdot \vec{N}^{m,p} \right\rangle_{\vec{i}}^{n+1} \left\langle \phi^{\vec{j}_m} \right\rangle_{\vec{i}} \omega_{\vec{i}}^p \\
  &\quad + \sum_{m \in M^l} \sum_{p \in P_R^m} \sum_{\vec{i} \in J_b^p} \left(\frac{\gamma}{\beta \Delta t} \langle b_{0,N}^m \rangle_{\vec{i}}^{n+1} \langle u_N^m \rangle_{\vec{i}}^{n+1} + \langle b_{1,N}^m \rangle_{\vec{i}}^{n+1} \langle u_N^m \rangle_{\vec{i}}^{n+1} \right) \langle \| \vec{N}^{m,p} \| \rangle_{\vec{i}} \left\langle \phi^{\vec{j}_m} \right\rangle_{\vec{i}} \omega_{\vec{i}}^p,
  \end{aligned}$$

  $$\begin{aligned}
  b_N^e(v_N^l) &= \sum_{m \in M^l} \sum_{\vec{i} \in J} \langle f_N^m \rangle_{\vec{i}}^{n+1} \left\langle \phi^{\vec{j}_m} \right\rangle_{\vec{i}} \langle |J_N^m| \rangle_{\vec{i}} \omega_{\vec{i}} \\
  &\quad + \sum_{m \in M^l} \sum_{p \in P_N^m} \sum_{\vec{i} \in J_b^p} \langle h_N^m \rangle_{\vec{i}}^{n+1} \langle \| \vec{N}^{m,p} \| \rangle_{\vec{i}} \left\langle \phi^{\vec{j}_m} \right\rangle_{\vec{i}} \omega_{\vec{i}}^p \\
  &\quad + \sum_{m \in M^l} \sum_{p \in P_R^m} \sum_{\vec{i} \in J_b^p} \langle q_N^m \rangle_{\vec{i}}^{n+1} \langle \| \vec{N}^{m,p} \| \rangle_{\vec{i}} \left\langle \phi^{\vec{j}_m} \right\rangle_{\vec{i}} \omega_{\vec{i}}^p \\
  &\quad - \sum_{m \in M^l} \sum_{\vec{i} \in J} \left(\langle c_N^m \rangle_{\vec{i}}^{n+1} \left\langle \tilde{u}_N^{(1),m} \right\rangle_{\vec{i}}^{n+1} - \frac{\gamma}{\beta \Delta t} \langle c_N^m \rangle_{\vec{i}}^{n+1} \langle \tilde{u}_N^m \rangle_{\vec{i}}^{n+1} - \frac{1}{\beta \Delta t^2} \langle \tilde{u}_N^m \rangle_{\vec{i}}^{n+1} \right) \left\langle \phi^{\vec{j}_m} \right\rangle_{\vec{i}} \langle |J_N^m| \rangle_{\vec{i}} \omega_{\vec{i}} \\
  &\quad - \sum_{m \in M^l} \sum_{p \in P_R^m} \sum_{\vec{i} \in J_b^p} \left(\langle b_{0,N}^m \rangle_{\vec{i}}^{n+1} \left\langle \tilde{u}_N^{(1),m} \right\rangle_{\vec{i}}^{n+1} - \frac{\gamma}{\beta \Delta t} \langle b_{0,N}^m \rangle_{\vec{i}}^{n+1} \langle \tilde{u}_N^m \rangle_{\vec{i}}^{n+1} \right) \langle \| \vec{N}^{m,p} \| \rangle_{\vec{i}} \left\langle \phi^{\vec{j}_m} \right\rangle_{\vec{i}} \omega_{\vec{i}}^p,
  \end{aligned}$$

  for $n \in J_t$.

- Correction step:
  Finally calculate:

$$\left\langle u_N^{(2)} \right\rangle_l^{n+1} = \frac{1}{\beta \Delta t^2} \left(\langle u_N \rangle_l^{n+1} - \langle \tilde{u}_N \rangle_l^{n+1} \right), \tag{5}$$

$$\left\langle u_N^{(1)} \right\rangle_l^{n+1} = \left\langle \tilde{u}_N^{(1)} \right\rangle_l^{n+1} + \gamma \Delta t \left\langle u_N^{(2)} \right\rangle_l^{n+1}, \tag{6}$$

for $l \in J^G \setminus J_{b,D}^G$ and $n \in J_t$.

Clearly, for the initial step we have $\langle u_N \rangle_l^0 = \langle u_{0,N} \rangle_l$, $l \in J^G$, $\langle u_N^{(1)} \rangle_l^0 = \langle u_{1,N} \rangle_l$, $l \in J^G \setminus J_{b,D}^G$, while the set of values $\{\langle u_N^{(2)} \rangle_l^0\}_{l \in J^G \setminus J_{b,D}^G}$ is computed as the approximation of the set $\{\langle \frac{\partial^2 u_N}{\partial t^2} \rangle_l^0\}_{l \in J^G \setminus J_{b,D}^G}$, which in turn is directly calculated from the semi-discrete modified variational formulation (4).

The above presented form is the classical formulation for implementing a member of the Newmark family of time integration methods. After intensive numerical experimentation, we detected a slight disadvantage of the proposed methodology, namely a significant increase of the roundoff error as $\Delta t \to 0$, which resulted in the complete loss of the theoretically predicted order of accuracy of the method. This is of minor importance since very small time steps are seldom used with implicit time integration schemes, but we believe that it is at least aesthetically pleasing for one to know that it is possible to achieve machine precision accuracy by decreasing the time step without having to worry about amplification of roundoff errors. Such a behavior can easily be avoided by a simple change at the correction step of the algorithm. To fix ideas, instead of using (5) to compute $\{\langle u_N \rangle_l^{n+1}\}_{l \in J^G \setminus J_{b,D}^G}$, we solve the semi-discretized variational formulation (4) for this set of values, after substituting the temporal derivatives with their discrete approximants and after using relation (6). This modified version of the correction step succeeds in preventing the accumulation of roundoff error as the time step decreases, but unfortunately demands a higher price to be paid in terms of computational efficiency and programming complexity.

The single most time consuming step in the above formulation, is the solution of the discrete elliptic boundary value problem at every distinct time level. An effective way of addressing such a problem in the framework of domain decomposition methods is the so-called influence matrix algorithm. A detailed presentation of application of such a method to fully discretized elliptic variational boundary value problems is included in [9]. Here, we only mention that by utilizing this kind of technique we are able to obtain the solution of the global system at the cost of two local solutions in each subdomain, plus a solution of a problem concerning the interface and some of the boundary values, plus the computation of the discrete Green's functions and the formation of the components of the influence matrix, which is usually performed in a preprocessing stage of the calculations. For the solution of the linear algebraic systems that result from the above decoupling procedure, we have chosen to apply the standard LU-factorization method in collaboration with the efficient matrix-diagonalization technique (whenever the form of the specific problem allowed us to do so), although other algorithms could have been considered as well.

Before ending this subsection, let us mention some important modifications that have to take place in the special case of axisymmetric acoustic wave simulations. When the spatial differential operator is the Laplacian one in cylindrical coordinates and axial symmetry is assumed, then we have:

$$L = -c_0^2 \left(\frac{\partial^2}{\partial x^2} + \frac{\partial^2}{\partial y^2} + \frac{1}{y} \frac{\partial}{\partial y} \right), \tag{7}$$

with $c_0 \in \Re$ the constant wave speed and (x,y) the axial and radial coordinates, respectively. On the axis of symmetry ($y = 0$) a boundary condition must be specified so that the problem to have a unique bounded solution. This "symmetry condition" has the form of a homogeneous Neumann boundary condition,

namely $\frac{\partial u}{\partial n_L} = 0$. In the weak collocation formulation of the problem, the imposition of Neumann and Robin boundary operators at the discrete level involves the computation of the pseudospectral residual of the partial differential equation on the given grid node. In view of the fact that L has a simple pole singularity at $y = 0$, we are obliged to modify the semi-discrete variational statement of the initial boundary value problem, before proceeding to the temporal discretization. The modified formulation of the linear functionals that appear in (4), reads:

$$a_N(t; u_N, v_N^l) = \sum_{m \in M^l} \sum_{\vec{i} \in J} \left(\langle y^m \rangle_{\vec{i}} \frac{d^2 \langle u_N^m \rangle_{\vec{i}}}{dt^2} + \langle y^m \rangle_{\vec{i}} \langle c_N^m \rangle_{\vec{i}} \frac{d \langle u_N^m \rangle_{\vec{i}}}{dt} + \langle y^m L_N^m[u_N^m] \rangle_{\vec{i}} \right) \left\langle \phi^{\vec{j}_m} \right\rangle_{\vec{i}} \langle |J_N^m| \rangle_{\vec{i}} \omega_{\vec{i}}$$

$$+ \sum_{m \in M^l} \sum_{p=1}^{4} \sum_{\vec{i} \in J_b^p} \langle y^m \rangle_{\vec{i}} \left\langle \vec{D}_{L_N}^m[u_N^m] \cdot \vec{N}^{m,p} \right\rangle_{\vec{i}} \left\langle \phi^{\vec{j}_m} \right\rangle_{\vec{i}} \omega_{\vec{i}}^p$$

$$+ \sum_{m \in M^l} \sum_{p \in P_R^m} \sum_{\vec{i} \in J_b^p} \left(\langle y^m \rangle_{\vec{i}} \langle b_{0,N}^m \rangle_{\vec{i}} \frac{d \langle u_N^m \rangle_{\vec{i}}}{dt} + \langle y^m \rangle_{\vec{i}} \langle b_{1,N}^m \rangle_{\vec{i}} \langle u_N^m \rangle_{\vec{i}} \right) \left\langle \left\| \vec{N}^{m,p} \right\| \right\rangle_{\vec{i}} \left\langle \phi^{\vec{j}_m} \right\rangle_{\vec{i}} \omega_{\vec{i}}^p,$$

$$b_N(t; v_N^l) = \sum_{m \in M^l} \sum_{\vec{i} \in J} \langle y^m \rangle_{\vec{i}} \langle f_N^m \rangle_{\vec{i}} \left\langle \phi^{\vec{j}_m} \right\rangle_{\vec{i}} \langle |J_N^m| \rangle_{\vec{i}} \omega_{\vec{i}}$$

$$+ \sum_{m \in M^l} \sum_{p \in P_N^m} \sum_{\vec{i} \in J_b^p} \langle y^m \rangle_{\vec{i}} \langle h_N^m \rangle_{\vec{i}} \left\langle \left\| \vec{N}^{m,p} \right\| \right\rangle_{\vec{i}} \left\langle \phi^{\vec{j}_m} \right\rangle_{\vec{i}} \omega_{\vec{i}}^p$$

$$+ \sum_{m \in M^l} \sum_{p \in P_R^m} \sum_{\vec{i} \in J_b^p} \langle y^m \rangle_{\vec{i}} \langle q_N^m \rangle_{\vec{i}} \left\langle \left\| \vec{N}^{m,p} \right\| \right\rangle_{\vec{i}} \left\langle \phi^{\vec{j}_m} \right\rangle_{\vec{i}} \omega_{\vec{i}}^p.$$

By utilizing such a technique, the pole singularity of the spatial differential operator is efficiently eliminated, while the spaces of trial and test functions remain unchanged. After these modifications, we are in the position of applying a member of the Newmark family of schemes, in order to integrate in time the system of semi-discretized equations. From the above stated forms, it is easily concluded that when axisymmetric problems are considered, only the sets of values $\{\langle y \rangle_l \langle u_N^{(1)} \rangle_l\}_{l \in J^G \setminus J_{b,D}^G}, \{\langle y \rangle_l \langle u_N^{(2)} \rangle_l\}_{l \in J^G \setminus J_{b,D}^G}, \{\langle y \rangle_l \langle \tilde{u}_N^{(1)} \rangle_l\}_{l \in J^G \setminus J_{b,D}^G}$ and $\{\langle y \rangle_l \langle \tilde{u}_N \rangle_l\}_{l \in J^G \setminus J_{b,D}^G}$ need to be calculated at the prediction and correction steps of the temporal approximation algorithm at every discrete time level.

4.2. Runge–Kutta–Nyström method

In the present subsection, we employ a high order explicit Runge–Kutta–Nyström method in order to discretize the temporal differential operators. Having in mind that the wave field along with its temporal derivatives of the first two orders are continuous throughout $\bar{\Omega}$ for all times, namely $u_N(t), \frac{\partial u_N}{\partial t}(t), \frac{\partial^2 u_N}{\partial t^2}(t) : I \to C^0(\bar{\Omega})$, we are able to reformulate the semi-discrete modified variational statement (4) into the following explicit system of ordinary differential equations:

$$\left\|
\begin{array}{l}
\frac{d^2 \langle u_N \rangle_l}{dt^2}(t) = F_l\left(t, \langle u_N \rangle_k(t), \frac{d \langle u_N \rangle_k}{dt}(t)\right), \quad l \in J^G \setminus J_{b,D}^G, \ k \in J^G, \ t \in I, \\
\langle u_N \rangle_l(t) = \langle g_N \rangle_l(t), \quad l \in J_{b,D}^G, \ t \in I, \\
\langle u_N \rangle_l(0) = \langle u_{0,N} \rangle_l, \quad l \in J^G, \\
\frac{d \langle u_N \rangle_l}{dt}(0) = \langle u_{1,N} \rangle_l, \quad l \in J^G,
\end{array}
\right.$$

where the precise form of the functions $F_l, l \in J^G \setminus J_{b,D}^G$ is assumed to be known.

Before proceeding with the detailed presentation of the temporal integrator, let us comment that a disturbing feature of applying explicit Runge–Kutta methods to initial boundary value problems discretized by the method of lines, is the loss of accuracy (or order reduction of the algorithm if you prefer) that stems from the wrong specification of boundary conditions at the intermediate stages of the integration procedure (see [17,18]). In our case, since the Neumann and Robin boundary operators are naturally included in the modified variational formulation, this problem arises only for the nodes that belong to the Dirichlet boundary. A known remedy for the solution of such problems is to enforce an extension of the inner Runge–Kutta scheme on the boundary, while ignoring the given boundary condition (see for instance [17]). This technique cannot be applied in collaboration with the weak collocation method for the spatial approximation, because the test functions of the variational formulation are identically equal to zero on the portion of the boundary where Dirichlet conditions are to be enforced. In order to cope with this situation, which arises whenever the weak formalism and an explicit Runge–Kutta–Nyström method must be simultaneously applied, we suggest a suitable projection of the partial differential equation on the finite-dimensional space spanned by the global Lagrange basis $\{v_N^l(\vec{x})\}_{l \in J_{b,D}^G}$. The precise semi-discrete statement reads:

$$\sum_{m \in M^l} \sum_{\vec{i} \in J} \left(\frac{\mathrm{d}^2 \langle u_N^m \rangle_{\vec{i}}}{\mathrm{d}t^2} + \langle c_N^m \rangle_{\vec{i}} \frac{\mathrm{d}\langle u_N^m \rangle_{\vec{i}}}{\mathrm{d}t} + \langle L_N^m[u_N^m] \rangle_{\vec{i}} - \langle f_N^m \rangle_{\vec{i}} \right) \left\langle \phi^{\vec{j}_m} \right\rangle_{\vec{i}} \langle |J_N^m| \rangle_{\vec{i}} \omega_{\vec{i}} = 0, \tag{8}$$

for all $l \in J_{b,D}^G$ with $l = G(m, \vec{j}_m)$, $\vec{j}_m \in J$, $m \in M^l$, and it is to be used only for the computation of values involved in the intermediate stages of the Runge–Kutta–Nyström method. Relation (8) gives us the opportunity of extending the family of functions $\{F_l\}_{l \in J^G \setminus J_{b,D}^G}$ so as to include new members defined for $l \in J_{b,D}^G$. Although this treatment is illustrated in the framework of the weak Legendre collocation method for the spatial approximation, we believe that the idea is widely applicable, and can be generally combined with methods that discretize the variational formulation of the initial boundary value problem, especially with the ones that use a Lagrangian system of basis functions. Moreover, it can be utilized even when the partial differential equation is of first order in time and also if the spatial operator is nonlinear.

We now discuss the precise formulation of a classic Runge–Kutta–Nyström method of fourth order for the temporal approximation (see [19]). Let us define four sets of auxiliary variables as $\{K_l^i\}_{l \in J^G}$, $i = 1, \ldots, 4$. If the enriched family of functions $\{F_l\}_{l \in J^G}$ has a dependence on first-order temporal derivatives, then the proposed algorithm obtains the following form (keeping in mind that $\frac{\mathrm{d}\langle u_N \rangle_k}{\mathrm{d}t} = \langle \frac{\partial u_N}{\partial t} \rangle_k$, $k \in J^G$):

- Intermediate steps:
  For each discrete time level and for all spatial nodes calculate:

$$K_l^1 = F_l\left(t^n, \langle u_N \rangle_k^n, \left\langle \frac{\partial u_N}{\partial t} \right\rangle_k^n \right),$$

$$K_l^2 = F_l\left(t^n + \frac{\Delta t}{2}, \langle u_N \rangle_k^n + \frac{\Delta t}{2} \left\langle \frac{\partial u_N}{\partial t} \right\rangle_k^n + \frac{\Delta t^2}{8} K_k^1, \left\langle \frac{\partial u_N}{\partial t} \right\rangle_k^n + \frac{\Delta t}{2} K_k^1 \right),$$

$$K_l^3 = F_l\left(t^n + \frac{\Delta t}{2}, \langle u_N \rangle_k^n + \frac{\Delta t}{2} \left\langle \frac{\partial u_N}{\partial t} \right\rangle_k^n + \frac{\Delta t^2}{8} K_k^1, \left\langle \frac{\partial u_N}{\partial t} \right\rangle_k^n + \frac{\Delta t}{2} K_k^2 \right),$$

$$K_l^4 = F_l\left(t^n + \Delta t, \langle u_N \rangle_k^n + \Delta t \left\langle \frac{\partial u_N}{\partial t} \right\rangle_k^n + \frac{\Delta t^2}{2} K_k^3, \left\langle \frac{\partial u_N}{\partial t} \right\rangle_k^n + K_k^3 \right),$$

  for all $l \in J^G$, where $k \in J^G$ and $n \in J_t$.

- Update step:
Calculate the values of the wave field and of its first-order time derivative on every node which does not belong to the Dirichlet portion of the boundary, as:

$$\langle u_N \rangle_l^{n+1} = \langle u_N \rangle_l^n + \Delta t \left\{ \left\langle \frac{\partial u_N}{\partial t} \right\rangle_l^n + \frac{\Delta t}{6} \left(K_l^1 + K_l^2 + K_l^3 \right) \right\},$$

$$\left\langle \frac{\partial u_N}{\partial t} \right\rangle_l^{n+1} = \left\langle \frac{\partial u_N}{\partial t} \right\rangle_l^n + \frac{\Delta t}{6} \left(K_l^1 + 2K_l^2 + 2K_l^3 + K_l^4 \right),$$

for all $l \in J^{\mathrm{G}} \setminus J_{\mathrm{b},D}^{\mathrm{G}}$ and each $n \in J_t$. For the grid points on the Dirichlet boundary, compute:

$$\langle u_N \rangle_l^{n+1} = \langle g_N \rangle_l^{n+1},$$

$$\left\langle \frac{\partial u_N}{\partial t} \right\rangle_l^{n+1} = \left\langle \frac{\partial g_N}{\partial t} \right\rangle_l^{n+1},$$

for all $l \in J_{\mathrm{b},D}^{\mathrm{G}}$ and each $n \in J_t$.

If the functions $\{F_l\}_{l \in J^{\mathrm{G}}}$ do not depend on the first-order temporal derivative of the wave field, then the third argument of these functions does no longer exist and one of the four sets of auxiliary variables ceases to be necessary for the overall formulation. For the first step, we use the initial conditions $\langle u_N \rangle_l^0 = \langle u_{0,N} \rangle_l$ and $\langle \frac{\partial u_N}{\partial t} \rangle_l^0 = \langle u_{1,N} \rangle_l$, $\forall l \in J^{\mathrm{G}}$, in order to start the algorithm. Please note that although the Dirichlet boundary conditions are completely ignored at the intermediate steps (as they are replaced by (8)), they are strongly enforced at the updating step along with their first-order temporal derivative.

Before closing this subsection, let us address the subject of the "apparent" singularity which arises when cylindrical axially symmetric problems are considered. As we have already mentioned, the actual difficulty lays in attempting to enforce the discrete condition on the symmetry axis, since this involves the collocation of the singular spatial differential operator of the partial differential equation. Unfortunately, a technique similar to the one proposed in the previous subsection cannot be applied when an explicit method like the Runge–Kutta–Nysröm is utilized, since the time integrator demands the sole presence of the second-order temporal derivative of the wave field at the left-hand side of the semi-discrete system of equations. Furthermore, we would prefer to avoid transforming the dependent wave variable, like done in [20], because with such a method the recovering of the original wave field on the symmetry axis becomes a very difficult (if not impossible) task in general subdomain topologies due to the irreversibility of the transformation performed. Remedies for similar problems which mainly involve the integration of the Navier–Stokes equations in cylindrical geometries for both incompressible as well as compressible flows, are presented in [21–23]. In this work, we adopt a method similar to the one proposed by Constantinescu and Lele in [24] but in a rather different context. Let us temporarily shift to the three dimensional setting of a wave propagation problem in cylindrical coordinates. Applying the parity theorem stated by Boyd in [3], we can expand an arbitrary scalar function which is analytic at $y = 0$, as a Fourier series in the polar angle z, in the following way:

$$u(x,y,z,t) = \sum_{\mu=0}^{\infty} \left\{ U_{a,\mu}(x,y,t) \cos(\mu z) + U_{b,\mu}(x,y,t) \sin(\mu z) \right\},$$

where:

$$U_{a,\mu}(x,y,t) = y^\mu \sum_{\lambda=0}^{\infty} A_{\mu\lambda}(x,t) y^{2\lambda},$$

$$U_{b,\mu}(x,y,t) = y^\mu \sum_{\lambda=0}^{\infty} B_{\mu\lambda}(x,t) y^{2\lambda}.$$

When axial symmetry is assumed (in the sense that the functions involved have no dependence on the polar angle), we deduce from the above series representation that $U_{a,\mu} = U_{b,\mu} = 0$ for all $\mu \geqslant 1$ and so:

$$u(x,y,t) = U_{a,0}(x,y,t) = \sum_{\lambda=0}^{\infty} A_{0\lambda}(x,t) y^{2\lambda}.$$

It is easy to confirm that:

$$\frac{\partial u}{\partial y}(x,y,t) = \sum_{\lambda=1}^{\infty} 2\lambda A_{0\lambda}(x,t) y^{2\lambda-1},$$

$$\frac{\partial^2 u}{\partial y^2}(x,y,t) = \sum_{\lambda=1}^{\infty} 2\lambda(2\lambda - 1) A_{0\lambda}(x,t) y^{2\lambda-2},$$

and consequently:

$$\lim_{y\to 0} \left(\frac{\partial u}{\partial y} \right) = 0,$$

$$\lim_{y\to 0} \left(\frac{1}{y} \frac{\partial u}{\partial y} \right) = \lim_{y\to 0} \left(\frac{\partial^2 u}{\partial y^2} \right) = 2A_{01}.$$

The former of the previous relations recovers the homogeneous Neumann boundary condition we impose on the symmetry axis, while the latter lets us conclude that:

$$\lim_{y\to 0} L[u] = \lim_{y\to 0} \left\{ -c_0^2 \left(\frac{\partial^2 u}{\partial x^2} + 2\frac{\partial^2 u}{\partial y^2} \right) \right\}, \tag{9}$$

for any arbitrary analytic function u at $y = 0$, with L the spatial operator given by (7). Expression (9) can be viewed as an application of L'Hôpital's rule on the singular term of the spatial differential operator (see [25]), which enables us to resolve the singularity problem that arises from the cooperation between the weak collocation and the explicit Runge–Kutta–Nysröm method for the numerical simulation of axisymmetric wave propagation problems.

5. Numerical wave simulations

In this section, we present a variety of pseudospectral wave solutions in order to argue in favor of the efficiency and robustness of the proposed methodology. In general, we validated both the spatial and the temporal approximation methods for the solution of initial boundary value problems with mixed boundary conditions, in different subdomain topologies. We began by using an exact two-dimensional standing wave solution so as to test the algorithm in a single domain setting, as well as in an unstructured subdomain partition. Then, we studied the convergence properties of the different schemes by computing a traveling plane wave solution of the acoustic wave equation and examined the perform-

ance of the various methods in complex curvilinear geometries. Subsequently, we proceeded by solving for two axisymmetric analytical solutions and confirmed the efficiency of our proposed modifications for axially symmetric evolution partial differential equations. Afterwards, we concerned ourselves with the dissipation and dispersion error behavior of the numerical schemes, and studied the spatial and temporal resolution requirements for the computation of plane wave solutions. Up to this point, we have only dealt with exact solutions of model problems. Next, we present wave propagation results in unbounded domains with utilization of absorbing boundary conditions and properly formulated dissipative wave operators. Finally, we performed an axisymmetric acoustic pulse evolution simulation in a constricted tube, while comparing our results in terms of accuracy and computer code efficiency, with a well-established spectral collocation form of the discontinuous Galerkin method. The theoretical convergence rates of the spatial and temporal discretization schemes were generally verified by the computational results.

Before we actually proceed with the specific numerical examples, we should comment, for a while, on the norms used for the convergence studies and for general comparison purposes. Suppose that X is a B-space defined over Ω and set a scalar function as $\psi : \Omega_I \to \Re$, with $\psi(t) : I \to X(\Omega)$. By determining the B-space X and consequently its norm function $\|\|_X$, we can safely compare two different elements of X, namely $\psi_a(t), \psi_b(t) : I \to X(\Omega)$, just by calculating the metric (or "distance") function $d_X(\psi_a, \psi_b) = \|\psi_a - \psi_b\|_X$ at any time level we wish the comparison to be performed. Next, we present the (time-dependent) discrete form of the specific norms to be used in the following subsections:

$$\|\psi\|_{N,L^\infty} = \max_{l \in J^G} \left\{ \langle |\psi| \rangle_l \right\} \quad \text{with } \psi(t) : I \to C^0(\bar{\Omega}),$$

$$\|\psi\|_{N,L^1} = \sum_{m \in M} \sum_{\vec{i} \in J} \langle |\psi^m| \rangle_{\vec{i}} \langle |J_N^m| \rangle_{\vec{i}} \omega_{\vec{i}} \quad \text{for } \psi^m(t) : I \to C^0(\bar{D}) \text{ and } m \in M,$$

$$\|\psi\|_{N,L^2} = \left\{ \sum_{m \in M} \sum_{\vec{i} \in J} \left(\langle \psi^m \rangle_{\vec{i}} \right)^2 \langle |J_N^m| \rangle_{\vec{i}} \omega_{\vec{i}} \right\}^{1/2} \quad \text{for } \psi^m(t) : I \to C^0(\bar{D}) \text{ and } m \in M,$$

$$\|\psi\|_{N,H^1} = \left\{ \sum_{m \in M} \sum_{\vec{i} \in J} \left[\left(\langle \psi^m \rangle_{\vec{i}} \right)^2 + \left(\left\langle \frac{\partial \psi^m}{\partial x} \right\rangle_{\vec{i}} \right)^2 + \left(\left\langle \frac{\partial \psi^m}{\partial y} \right\rangle_{\vec{i}} \right)^2 \right] \langle |J_N^m| \rangle_{\vec{i}} \omega_{\vec{i}} \right\}^{1/2},$$

with $\psi^m(t) : I \to C^1(\bar{D})$ and $m \in M$. The subscript N on the norm symbols is used to denote the fact that the previous forms constitute an equivalent discretized formulation of the standard norm functions of the L^∞, L^1, L^2 and H^1 B-spaces, respectively. The same subscript is used on the notations of the corresponding metrics.

Finally, let us note that in all subsequent numerical simulations we used the Runge–Kutta–Nyström method for the spatial convergence studies, so as to take advantage of its inherent high order accuracy. Moreover, we ensured that the temporal discretization errors were kept negligible whenever we tested the spatial accuracy of the method and vice versa. All of the results to be shown in this article were obtained on a 2.4 GHz Pentium Personal Computer.

5.1. Two-dimensional standing wave

For the beginning of the numerical experiments, we employed the proposed methodologies in order to solve the non-homogeneous initial boundary value problem:

$$\left\| \begin{array}{l} \frac{\partial^2 u}{\partial t^2} - c_0^2 \left(\frac{\partial^2 u}{\partial x^2} + \frac{\partial^2 u}{\partial y^2} \right) = U_0 \left[c_0^2 \left(\kappa_x^2 + \kappa_y^2 \right) - \omega^2 \right] \sin(\omega t) \sin(\kappa_x x) \sin(\kappa_y y) \quad \text{on } \Omega_I, \\ \quad u = 0 \quad \text{on } \Omega \text{ for } t = 0, \\ \frac{\partial u}{\partial t} = U_0 \omega \sin(\kappa_x x) \sin(\kappa_y y) \quad \text{on } \Omega \text{ for } t = 0, \\ \quad u = 0 \quad \text{on } \Gamma_D \times I, \\ \frac{\partial u}{\partial n_L} = c_0^2 U_0 \kappa_x \sin(\omega t) \cos(\kappa_x x) \sin(\kappa_y y) \quad \text{on } \Gamma_{N,1} \times I, \\ \frac{\partial u}{\partial n_L} = c_0^2 U_0 \kappa_y \sin(\omega t) \sin(\kappa_x x) \cos(\kappa_y y) \quad \text{on } \Gamma_{N,2} \times I, \end{array} \right.$$

with:

$$\Gamma_D = \{(x,y) \in \partial\Omega \,|\, x = 0, y \in (0, L_y)\} \cup \{(x,y) \in \partial\Omega \,|\, x \in (0, L_x), y = 0\},$$

$$\Gamma_{N,1} = \{(x,y) \in \partial\Omega \,|\, x = L_x, y \in (0, L_y)\},$$

$$\Gamma_{N,2} = \{(x,y) \in \partial\Omega \,|\, x \in (0, L_x), y = L_y\},$$

where (x,y) are the spatial coordinates in a Cartesian frame of reference, c_0 is the constant wave speed and $\Gamma_N = \Gamma_{N,1} \cup \Gamma_{N,2}$ with $\Gamma_{N,1} \cap \Gamma_{N,2} = \emptyset$. The spatial computational domain was $\Omega = (0, L_x) \times (0, L_y)$, with $L_x, L_y \in \Re$ and $L_x, L_y > 0$. The source term, initial and boundary conditions were such that the above stated problem was solved by the following exact infinitely differentiable stationary wave solution:

$$u_E(x,y,t) = U_0 \sin(\omega t) \sin(\kappa_x x) \sin(\kappa_y y),$$

with $U_0, \kappa_x, \kappa_y, \omega \in \Re$. In the following simulations, we used $\kappa_x = \kappa_y = \pi$, $L_x = L_y = 2$, $U_0 = 1$ and $\omega = 1$.

The problem was first solved by utilizing the monodomain version of the method. We used a unitary wave speed and a final time $T = 1$ for this specific test case. The convergence of the spatial error of the weak collocation approximation was exponential, as demonstrated in Fig. 1. Concerning the temporal behavior of the different schemes, the corresponding absolute errors are presented in Tables 1–3 for the Runge–Kutta–Nyström, the Newmark and the modified Newmark methods, respectively. Double precision accuracy was achieved by the fourth-order Runge–Kutta–Nyström method. As noted previously, the Newmark method failed to deliver the theoretically predicted second-order convergence rate in the limit $\Delta t \to 0$. On the other hand, the results of the modified version were not corrupted by the roundoff errors and managed to retain full second-order accuracy.

Next, we solved the same partial differential equation on an unstructured subdomain configuration shown in Fig. 2. We used $c_0 = 5$, Dirichlet boundary conditions on all of the computational border and fixed the time interval as $I = (0.0, 0.2)$. Infinite order spatial convergence was achieved by the spectral method, as illustrated in Fig. 3. The results of the modified Newmark method for the time integration are displayed in Table 4 and confirm the second-order temporal convergence rate of this scheme in a complex subdomain topology.

This test case enabled us to validate all the methodologies proposed, in a rectangular geometry configuration. The monodomain method gave satisfactory results for a mixed Dirichlet–Neumann initial boundary value problem, while the multidomain algorithm succeeded in a truly unstructured subdomain partition. The Runge–Kutta–Nyström time integrator delivered full fourth-order accuracy and finally, the modified Newmark method managed to surmount the problems faced by the classical implementation of the algorithm and stand up to the theoretical predictions.

5.2. Two-dimensional traveling wave

As a second numerical example, we considered a traveling plane wave solution of the acoustic wave equation. By the aid of this test case, we were able to study the convergence properties of the method in
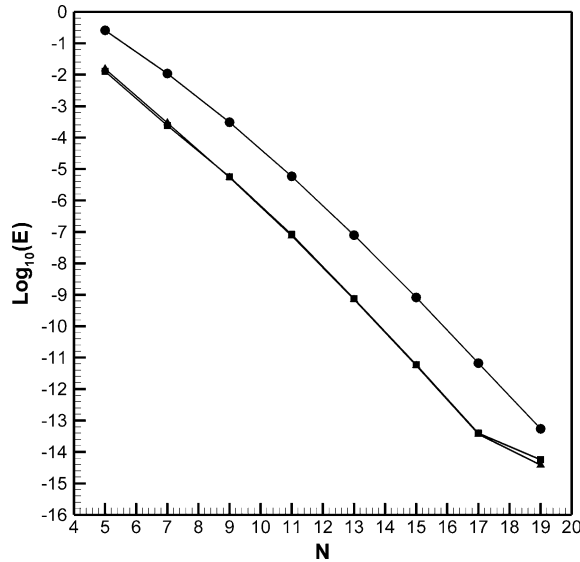
Fig. 1. Convergence plot for the two-dimensional standing wave problem at $t = 1.0$. Monodomain topology ($\blacksquare$) $E = d_{N,L^\infty}(u_N, u_E)$, ($\blacktriangle$) $E = d_{N,L^2}(u_N, u_E)$ and ($\bullet$) $E = d_{N,H^1}(u_N, u_E)$.

Table 1
Temporal accuracy results for the two-dimensional standing wave problem at $t = 1.0$ (monodomain topology and Runge–Kutta–Nyström method)

Δt	$d_{N,L^\infty}(u_N, u_E)$	$d_{N,L^2}(u_N, u_E)$	$d_{N,H^1}(u_N, u_E)$
10^{-1}	7.72×10^{-4}	5.84×10^{-4}	1.06×10^{-2}
10^{-2}	3.80×10^{-10}	2.72×10^{-10}	2.53×10^{-9}
10^{-3}	5.19×10^{-14}	2.64×10^{-14}	2.30×10^{-13}

Table 2
Temporal accuracy results for the two-dimensional standing wave problem at $t = 1.0$ (monodomain topology and Newmark method)

Δt	$d_{N,L^\infty}(u_N, u_E)$	$d_{N,L^2}(u_N, u_E)$	$d_{N,H^1}(u_N, u_E)$
10^{-1}	2.64×10^{-4}	2.12×10^{-4}	9.25×10^{-4}
10^{-2}	2.67×10^{-6}	2.14×10^{-6}	9.29×10^{-6}
10^{-3}	2.66×10^{-8}	2.13×10^{-8}	9.24×10^{-8}
10^{-4}	1.65×10^{-8}	1.60×10^{-8}	5.74×10^{-8}
10^{-5}	1.78×10^{-6}	1.73×10^{-6}	6.26×10^{-6}

Table 3
Temporal accuracy results for the two-dimensional standing wave problem at $t = 1.0$ (monodomain topology and modified Newmark method)

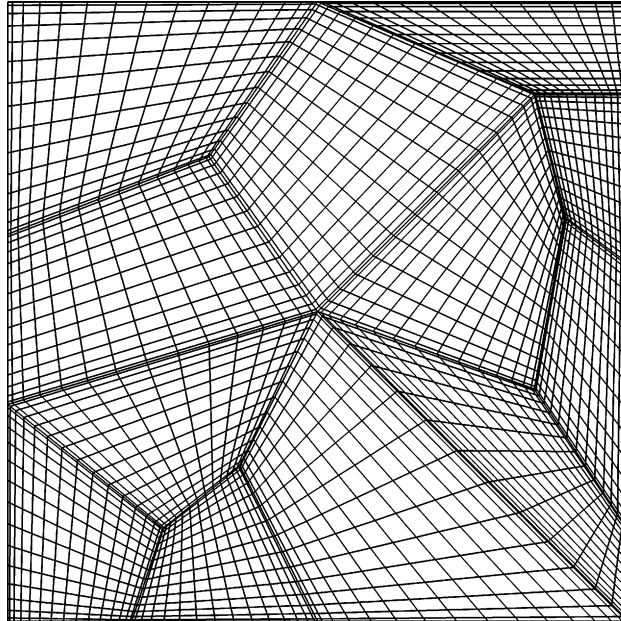| Δt	$d_{N,L^\infty}(u_N, u_E)$	$d_{N,L^2}(u_N, u_E)$	$d_{N,H^1}(u_N, u_E)$
10^{-1}	2.64×10^{-4}	2.12×10^{-4}	9.25×10^{-4}
10^{-2}	2.67×10^{-6}	2.14×10^{-6}	9.29×10^{-6}
10^{-3}	2.67×10^{-8}	2.14×10^{-8}	9.29×10^{-8}
10^{-4}	2.67×10^{-10}	2.14×10^{-10}	9.28×10^{-10}
10^{-5}	9.82×10^{-12}	7.60×10^{-12}	2.35×10^{-11}

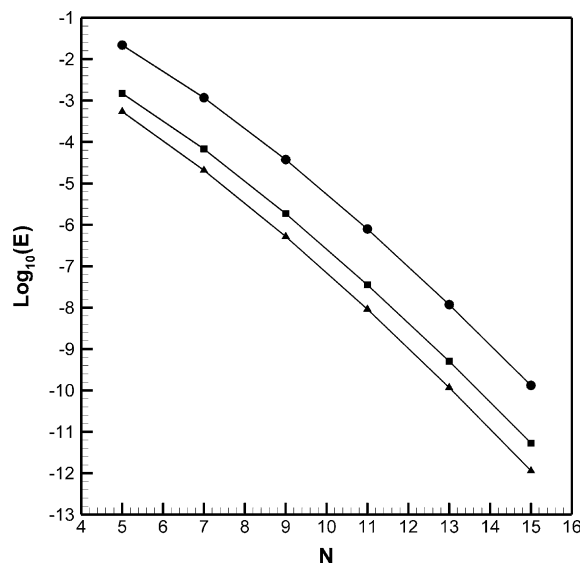Fig. 2. Unstructured grid with $N = 15$, for the two-dimensional standing wave problem.

Fig. 3. Convergence plot for the two-dimensional standing wave problem at $t = 0.2$. Unstructured subdomain topology (■) $E = d_{N,L^\infty}(u_N, u_E)$, (▲) $E = d_{N,L^2}(u_N, u_E)$ and (●) $E = d_{N,H^1}(u_N, u_E)$.

a wave propagation problem, while exploring its performance in both simple as well as complicated geo-metrical settings. The specific form of the initial boundary value problem was:

Table 4
Temporal accuracy results for the two-dimensional standing wave problem at $t = 0.2$ (unstructured subdomain topology and modified Newmark method)

Δt	$d_{N,L^\infty}(u_N, u_E)$	$d_{N,L^2}(u_N, u_E)$	$d_{N,H^1}(u_N, u_E)$
10^{-1}	8.51×10^{-6}	8.52×10^{-6}	3.88×10^{-5}
10^{-2}	3.68×10^{-7}	3.68×10^{-7}	1.68×10^{-6}
10^{-3}	3.70×10^{-9}	3.70×10^{-9}	1.68×10^{-8}
10^{-4}	3.70×10^{-11}	3.70×10^{-11}	1.68×10^{-10}

$$\left\| \begin{array}{l} \frac{\partial^2 u}{\partial t^2} - c_0^2 \left(\frac{\partial^2 u}{\partial x^2} + \frac{\partial^2 u}{\partial y^2} \right) = 0 \quad \text{on } \Omega_I, \\ u = U_0 \cos(\kappa_x x + \kappa_y y) \quad \text{on } \Omega \text{ for } t = 0, \\ \frac{\partial u}{\partial t} = U_0 \omega \sin(\kappa_x x + \kappa_y y) \quad \text{on } \Omega \text{ for } t = 0, \\ u = U_0 \cos(\kappa_x x + \kappa_y y - \omega t) \quad \text{on } \Gamma_D \times I, \\ \frac{\partial u}{\partial n_L} = c_0^2 U_0 \kappa_y \sin(\kappa_x x + \kappa_y y - \omega t) \quad \text{on } \Gamma_{N,1} \times I, \\ \frac{\partial u}{\partial n_L} = -c_0^2 U_0 \kappa_y \sin(\kappa_x x + \kappa_y y - \omega t) \quad \text{on } \Gamma_{N,2} \times I, \end{array} \right.$$

where:

$$\Gamma_D = \{(x,y) \in \partial\Omega \,|\, x = 0, y \in (0, L_y)\} \cup \{(x,y) \in \partial\Omega \,|\, x = L_x, y \in (0, L_y)\},$$

$$\Gamma_{N,1} = \{(x,y) \in \partial\Omega \,|\, x \in (0, L_x), y = 0\},$$

$$\Gamma_{N,2} = \{(x,y) \in \partial\Omega \,|\, x \in (0, L_x), y = L_y\}.$$

The analytical solution was given by the relation:

$$u_E(x, y, t) = U_0 \cos(\kappa_x x + \kappa_y y - \omega t),$$

with $\omega^2 = c_0^2(\kappa_x^2 + \kappa_y^2)$. The spatial domain was chosen to be $\Omega = (0, L_x) \times (0, L_y)$ and the parameters which determine the specific form of the problem and solution were set as $c_0 = 0.5$, $U_0 = 1$, $\kappa_x = \kappa_y = \sqrt{2}$, $L_x = L_y = 5$ and $\omega = 1$. We considered a four subdomain partition of the computational domain, comprised by orthogonal equally sized elements. For this simulation, we set the open time interval as $I = (0, 2)$. Spectral accuracy is presented for this plane wave solution in Fig. 4. Tables 5–7 display the convergence properties of the different temporal approximation methods. Once again the Runge–Kutta–Nyström method delivered fourth-order accuracy, while the modified version of the Newmark method succeeded in achieving second-order accuracy in contradiction with the traditional formulation. In general, the behavior of the multidomain method in the context of a wave propagation problem with mixed boundary conditions, was found to be very satisfying.

In order to address the issue of efficiency of the different time integration schemes, we present comparisons concerning CPU time, memory allocation and relative error norms. First, let us define C_t^{Me} to be the CPU time consumed per time step by each method, where "Me" stands for "RKN", "N" and "MN" symbolizing the Runge–Kutta–Nyström, the Newmark and the modified Newmark methods, respectively. In a similar manner, C_m^{Me} is used to denote the computer memory occupied by each one of the different schemes, while $C_e^{Me} = \frac{d_{N,L^2}(u_N, u_E)}{\|u_E\|_{N,L^2}}$ is defined as the relative error of the solution obtained by each method with respect to the L^2 norm. By forming the ratios:

$$\Lambda_{RKN,t}^{Me} = \frac{C_t^{Me}}{C_t^{RKN}}, \quad \Lambda_{RKN,m}^{Me} = \frac{C_m^{Me}}{C_m^{RKN}} \quad \text{and} \quad \Lambda_{RKN,e}^{Me} = \text{Log}_{10}\left(\frac{C_e^{Me}}{C_e^{RKN}}\right),$$
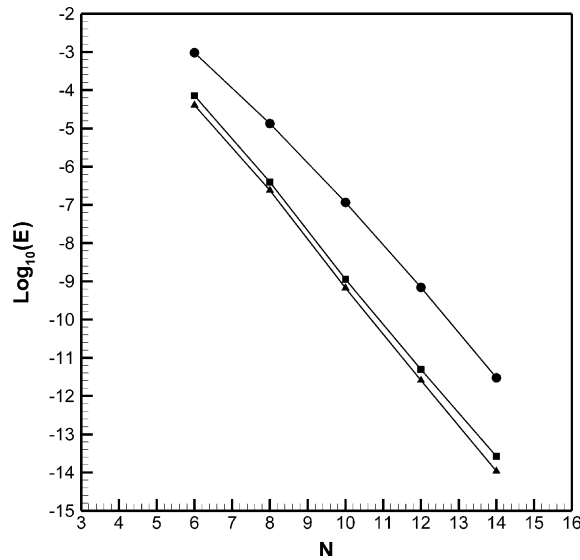
Fig. 4. Convergence plot for the two-dimensional traveling wave problem at $t = 2.0$. Four subdomain topology ($\blacksquare$) $E = \frac{d_{N,L^\infty}(u_N,u_E)}{\|u_E\|_{N,L^\infty}}$, ($\blacktriangle$) $E = \frac{d_{N,L^2}(u_N,u_E)}{\|u_E\|_{N,L^2}}$ and ($\bullet$) $E = \frac{d_{N,H^1}(u_N,u_E)}{\|u_E\|_{N,H^1}}$.

Table 5
Temporal accuracy results for the two-dimensional traveling wave problem at $t = 2.0$ (four subdomain topology and Runge–Kutta–Nyström method)

Δt	$d_{N,L^\infty}(u_N,u_E)/\|u_E\|_{N,L^\infty}$	$d_{N,L^2}(u_N,u_E)/\|u_E\|_{N,L^2}$	$d_{N,H^1}(u_N,u_E)/\|u_E\|_{N,H^1}$
10^{-1}	1.40×10^{-6}	6.22×10^{-7}	8.71×10^{-7}
10^{-2}	1.67×10^{-10}	6.05×10^{-11}	8.41×10^{-11}
10^{-3}	1.56×10^{-14}	6.82×10^{-15}	1.72×10^{-14}

Table 6
Temporal accuracy results for the two-dimensional traveling wave problem at $t = 2.0$ (four subdomain topology and Newmark method)

Δt	$d_{N,L^\infty}(u_N,u_E)/\|u_E\|_{N,L^\infty}$	$d_{N,L^2}(u_N,u_E)/\|u_E\|_{N,L^2}$	$d_{N,H^1}(u_N,u_E)/\|u_E\|_{N,H^1}$
10^{-1}	2.56×10^{-3}	1.59×10^{-3}	1.65×10^{-3}
10^{-2}	2.56×10^{-5}	1.60×10^{-5}	1.66×10^{-5}
10^{-3}	2.51×10^{-7}	1.58×10^{-7}	1.64×10^{-7}
10^{-4}	7.14×10^{-7}	2.18×10^{-7}	2.69×10^{-7}
10^{-5}	7.11×10^{-5}	2.10×10^{-5}	2.62×10^{-5}

Table 7
Temporal accuracy results for the two-dimensional traveling wave problem at $t = 2.0$ (four subdomain topology and modified Newmark method)

Δt	$d_{N,L^\infty}(u_N,u_E)/\|u_E\|_{N,L^\infty}$	$d_{N,L^2}(u_N,u_E)/\|u_E\|_{N,L^2}$	$d_{N,H^1}(u_N,u_E)/\|u_E\|_{N,H^1}$
10^{-1}	2.56×10^{-3}	1.59×10^{-3}	1.65×10^{-3}
10^{-2}	2.56×10^{-5}	1.60×10^{-5}	1.66×10^{-5}
10^{-3}	2.56×10^{-7}	1.60×10^{-7}	1.66×10^{-7}
10^{-4}	2.56×10^{-9}	1.59×10^{-9}	1.65×10^{-9}
10^{-5}	1.25×10^{-10}	4.94×10^{-11}	9.91×10^{-11}

we were in the position to study the performance of every one of the implicit temporal approximation methods relatively to the explicit Runge–Kutta–Nyström scheme. The mathematical setting of the problem was retained, while the time step $\Delta t = 0.0001$ was used by all methods for the specific simulations. Table 8 presents the results for the four subdomain partition of the computational domain, for different values of the degree of the approximating polynomial N in each element, while Table 9 contains similar results but for the case of constant $N = 10$ and different decompositions of the computational domain into square elements, with S_n denoting the total number of subdomains. It is rather obvious that the Runge–Kutta–Nyström algorithm was the most efficient in terms of CPU time, memory allocation and accuracy. The modified Newmark scheme was proven to be better than the conventional Newmark method on the subject of accuracy, but fell short if CPU time and memory usage were primarily considered, as expected. Before ending with the efficiency results, let us mention that the preprocessing operations of each algorithm were not included in the time measurements and comment that the inefficiency of the implicit schemes is generally balanced by their unconditional stability properties, which enable the use of larger time steps at the cost of lower accuracy.

Subsequently, we proceeded with the numerical solution of the same problem in a complex geometry configuration by utilizing a complicated subdomain partition of the computational domain which included curvilinear quadrilateral elements. The detailed mesh is plotted in Fig. 5 and is bounded by $[0, L_x] \times [0, L_y]$. This grid was chosen to show that the method can solve on complex curvilinear geometries without regard to the number of subdomains that come together at a point. For this simulation, we used $c_0 = 5$, only Dirichlet boundary conditions on the spatial domain border and set the final time T for our studies equal

Table 8
Computer code performance results for the two-dimensional traveling wave problem at $t = 2.0$ (four subdomain topology)

N	Me	$A_{\mathrm{RKN},t}^{\mathrm{Me}}$	$A_{\mathrm{RKN},m}^{\mathrm{Me}}$	$A_{\mathrm{RKN},e}^{\mathrm{Me}}$
6	N	0.98	1.38	0.0001
	MN	1.21	1.42	0.0000
8	N	1.15	1.37	0.0020
	MN	1.39	1.42	0.0000
10	N	1.29	1.38	2.2394
	MN	1.54	1.43	0.4126
12	N	1.40	1.39	4.8980
	MN	1.66	1.43	2.7951
14	N	1.51	1.41	7.1806
	MN	1.78	1.45	5.1493

Table 9
Computer code performance results for the two-dimensional traveling wave problem at $t = 2.0$ (constant degree of approximating polynomial $N = 10$)

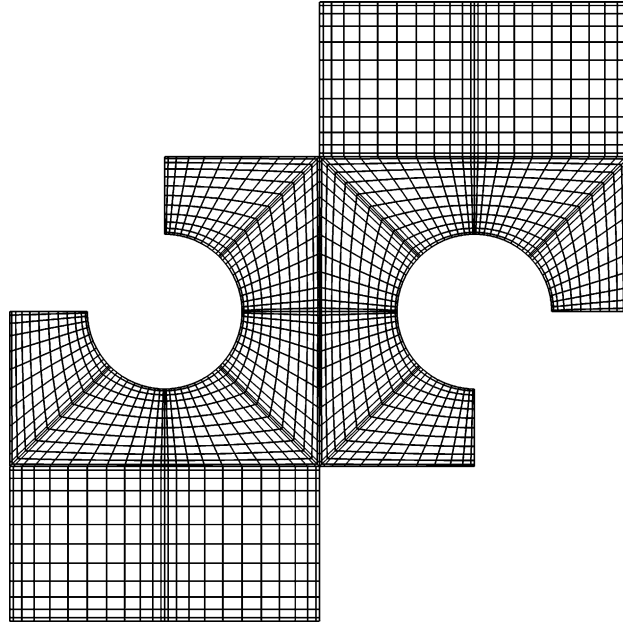| S_n	Me	$A_{\mathrm{RKN},t}^{\mathrm{Me}}$	$A_{\mathrm{RKN},m}^{\mathrm{Me}}$	$A_{\mathrm{RKN},e}^{\mathrm{Me}}$
1	N	1.18	1.34	0.0012
	MN	1.41	1.38	0.0000
4	N	1.29	1.38	2.2394
	MN	1.54	1.43	0.4126
9	N	1.46	1.48	3.9203
	MN	1.72	1.52	2.3225
16	N	1.73	1.86	5.4668
	MN	2.00	1.91	3.9415
25	N	2.08	2.56	6.1990
	MN	2.35	2.60	4.8062

Fig. 5. Complex geometry configuration for the two-dimensional traveling wave problem, with $N = 12$.

to 0.4. The results of the p-convergence study are displayed in Fig. 6, while the performance of the modified Newmark method for the temporal discretization is presented in Table 10. At this point, we feel necessary to note that at corner points where more than two subdomains meet, the present weak formulation of the pseudospectral method faced no difficulty in contrast with the customary strong formulation. Furthermore, not any kind of reflections or spurious modes were detected from the passage of the traveling wave through the interelement boundaries, as the dispersion and dissipation errors were kept at a very low level in the well resolved simulations.

5.3. Axisymmetric standing waves

In this subsection, we test the numerical methods in the context of smooth axisymmetric wave solutions. The first problem which was studied, had the following form:

$$\left\|\begin{array}{l} \frac{\partial^2 u}{\partial t^2} - c_0^2 \left(\frac{\partial^2 u}{\partial x^2} + \frac{\partial^2 u}{\partial y^2} + \frac{1}{y} \frac{\partial u}{\partial y} \right) = f \quad \text{on } \Omega_I, \\ u = U_0 \sinh(\kappa_x x) \cos(\kappa_y y) \quad \text{on } \Omega \text{ for } t = 0, \\ \frac{\partial u}{\partial t} = 0 \quad \text{on } \Omega \text{ for } t = 0, \\ u = U_0 \cos(\omega t) \sinh(\kappa_x x) \cos(\kappa_y y) \quad \text{on } \Gamma_D \times I, \\ \frac{\partial u}{\partial n_L} = 0 \quad \text{on } \Gamma_N \times I, \end{array}\right.$$

with:

$$\Gamma_D = \{(x,y) \in \partial\Omega \,|\, x = -L_x, y \in (0, L_y)\} \cup \{(x,y) \in \partial\Omega \,|\, x = L_x, y \in (0, L_y)\},$$

$$\Gamma_N = \{(x,y) \in \partial\Omega \,|\, x \in (-L_x, L_x), y = 0\} \cup \{(x,y) \in \partial\Omega \,|\, x \in (-L_x, L_x), y = L_y\},$$
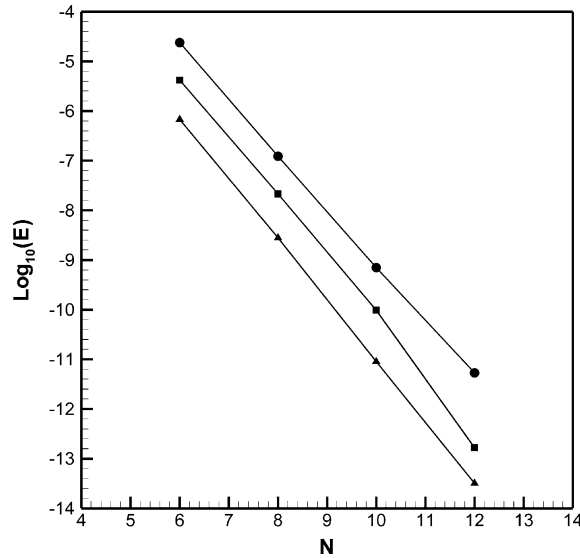
Fig. 6. Convergence plot for the two-dimensional traveling wave problem at $t = 0.4$. Complex subdomain topology (■) $E = \frac{d_{N,L^\infty}(u_N, u_E)}{\|u_E\|_{N,L^\infty}}$, (▲) $E = \frac{d_{N,L^2}(u_N, u_E)}{\|u_E\|_{N,L^2}}$ and (●) $E = \frac{d_{N,H^1}(u_N, u_E)}{\|u_E\|_{N,H^1}}$.

Table 10
Temporal accuracy results for the two-dimensional traveling wave problem at $t = 0.4$ (complex subdomain topology and modified Newmark method)

Δt	$d_{N,L^\infty}(u_N, u_E)/\|u_E\|_{N,L^\infty}$	$d_{N,L^2}(u_N, u_E)/\|u_E\|_{N,L^2}$	$d_{N,H^1}(u_N, u_E)/\|u_E\|_{N,H^1}$
10^{-1}	9.65×10^{-5}	4.60×10^{-5}	6.80×10^{-5}
10^{-2}	1.06×10^{-6}	4.17×10^{-7}	6.05×10^{-7}
10^{-3}	1.06×10^{-8}	4.17×10^{-9}	6.07×10^{-9}
10^{-4}	1.06×10^{-10}	4.17×10^{-11}	6.08×10^{-11}

where (x,y) are the axial and radial coordinates, respectively, in a cylindrical frame of reference. The computational domain assumed the form $\Omega = (-L_x, L_x) \times (0, L_y)$ and was initially partitioned in four orthogonal subdomains of equal area. The source term f at the partial differential equation, was defined so that the exact solution of the initial boundary value problem was:

$$u_E(x, y, t) = U_0 \cos(\omega t) \sinh(\kappa_x x) \cos(\kappa_y y).$$

In our simulations, the values $c_0 = 0.5$, $U_0 = 0.5$, $\kappa_x = 1$, $\kappa_y = \pi$, $L_x = L_y = 2$ and $\omega = 2\pi$ were utilized, while the final time for the computations was taken as $T = 1$. Fig. 7 clearly demonstrates the spectral convergence of the spatial approximation with polynomial order and Table 11 confirms the high order accuracy of the Runge–Kutta–Nyström method, as well as the success of modification (9) which was used for the imposition of the discrete equations on the axis of symmetry.

In the process of evaluating the convergence properties of the scheme with respect to the number of subdomains, let us define the mesh parameter:

$$h_s = \max\{\text{diam}(\Omega^m) \,|\, m \in M\},$$

which serves as an indicator of the element size. In the above expression, the diameter of the specific subdomain Ω^m is set as:
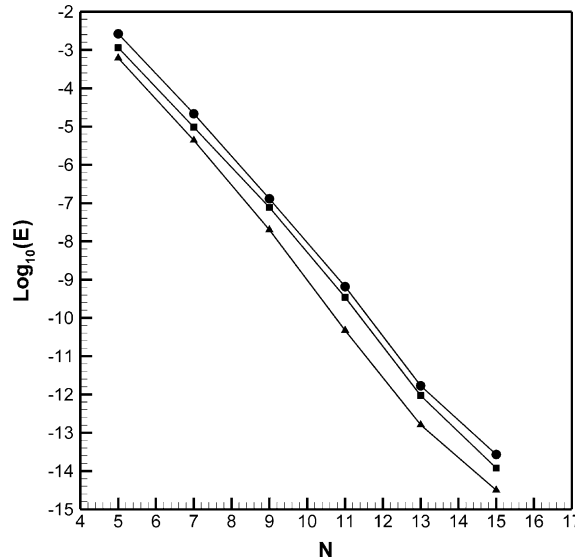
Fig. 7. Convergence plot for the axisymmetric standing wave problem at $t = 1.0$. Four subdomain topology ($\blacksquare$) $E = \frac{d_{N,L^\infty}(u_N,u_E)}{\|u_E\|_{N,L^\infty}}$, ($\blacktriangle$) $E = \frac{d_{N,L^2}(u_N,u_E)}{\|u_E\|_{N,L^2}}$ and ($\bullet$) $E = \frac{d_{N,H^1}(u_N,u_E)}{\|u_E\|_{N,H^1}}$.

Table 11
Temporal accuracy results for the axisymmetric standing wave problem at $t = 1.0$ (four subdomain topology and Runge–Kutta–Nyström method)

Δt	$d_{N,L^\infty}(u_N,u_E)/\|u_E\|_{N,L^\infty}$	$d_{N,L^2}(u_N,u_E)/\|u_E\|_{N,L^2}$	$d_{N,H^1}(u_N,u_E)/\|u_E\|_{N,H^1}$
10^{-1}	5.15×10^{-4}	4.04×10^{-4}	6.56×10^{-4}
10^{-2}	6.01×10^{-8}	4.15×10^{-8}	7.17×10^{-8}
10^{-3}	5.92×10^{-12}	4.15×10^{-12}	7.15×10^{-12}

$$\text{diam}(\Omega^m) = \sup\left\{\left\|\vec{x}_*^m - \vec{x}_{**}^m\right\| \,\middle|\, \vec{x}_*^m, \vec{x}_{**}^m \in \Omega^m\right\},$$

with $m \in M$, while $\|\|$ denotes the Euclidean norm function on $\Re^2$. At first, we considered the single element case and then sequentially divided the computational domain into 4, 9, 16 and 25 orthogonal subdomains, while retaining all the other simulation parameters of the previously considered mathematical problem and fixing h_s to be the common length of the diagonals of the individual elements. The domain decomposition was such that each subdomain assumed the following form:

$$\Omega^m = \left(-L_x + j_x \frac{2L_x}{\sqrt{S_n}}, -L_x + (j_x + 1)\frac{2L_x}{\sqrt{S_n}}\right) \times \left(j_y \frac{L_y}{\sqrt{S_n}}, (j_y + 1)\frac{L_y}{\sqrt{S_n}}\right),$$

with $m \in M$, $j_x, j_y = 0, \ldots, \sqrt{S_n} - 1$ and with S_n denoting the total number of elements. In this way, the dependence of h_s on S_n was given by:

$$h_s = \sqrt{\frac{4L_x^2 + L_y^2}{S_n}}.$$

Fig. 8 illustrates the convergence of the spatial discretization with respect to h_s, for four different values of the polynomial degree N. It is rather evident that the error did not decrease at a geometric rate. A least

squares fit to the logarithm of the relative L^2 error as a function of the logarithm of the mesh parameter, indicated the slopes 5.4468, 8.1963, 10.2625 and 11.8661, with correlation coefficients 0.9978, 0.9963, 0.9958 and 0.9943, for N equal to 5, 7, 9 and 11, respectively, so algebraic convergence of the approximation was obtained as expected.

We proceeded by solving another axial symmetric stationary wave problem, namely:

$$\left\| \begin{array}{l} \frac{\partial^2 u}{\partial t^2} - c_0^2 \left(\frac{\partial^2 u}{\partial x^2} + \frac{\partial^2 u}{\partial y^2} + \frac{1}{y} \frac{\partial u}{\partial y} \right) = f \quad \text{on } \Omega_I, \\ \quad u = 0 \quad \text{on } \Omega \text{ for } t = 0, \\ \frac{\partial u}{\partial t} = U_0 \omega \cos(\kappa_x x) \cos(\kappa_y y) \quad \text{on } \Omega \text{ for } t = 0, \\ u = U_0 \sin(\omega t) \cos(\kappa_x x) \cos(\kappa_y y) \quad \text{on } \Gamma_D \times I, \\ \frac{\partial u}{\partial n_L} = 0 \quad \text{on } \Gamma_N \times I, \end{array} \right.$$

with:

$$\Gamma_N = \{(x,y) \in \partial\Omega \,|\, x \in (0, L_x/2), y = 0\},$$

$$\Gamma_D : \bar{\Gamma}_D \cup \bar{\Gamma}_N = \partial\Omega, \Gamma_D \cap \Gamma_N = \emptyset.$$

The source function f, this time, was obtained by setting the analytical solution of the previously stated problem, as:

$$u_E(x,y,t) = U_0 \sin(\omega t) \cos(\kappa_x x) \cos(\kappa_y y).$$

The computational domain as well as the subdomain topology that we used were very similar to the ones depicted in Fig. 5, but transformed by a linear mapping in such a way so that at the end to have $0 \leqslant x \leqslant L_x$ and $0 \leqslant y \leqslant L_y$, with $L_x = L_y = 2$. In our calculations, we used $c_0 = 5$, $U_0 = 1$, $\kappa_x = \kappa_y = \pi$ and $\omega = 1$. Finally, the time interval was set as $I = (0.0, 0.2)$. Exponential convergence with order refinement was once again confirmed, as shown in Fig. 9. Table 12 displays the temporal convergence of the Newmark
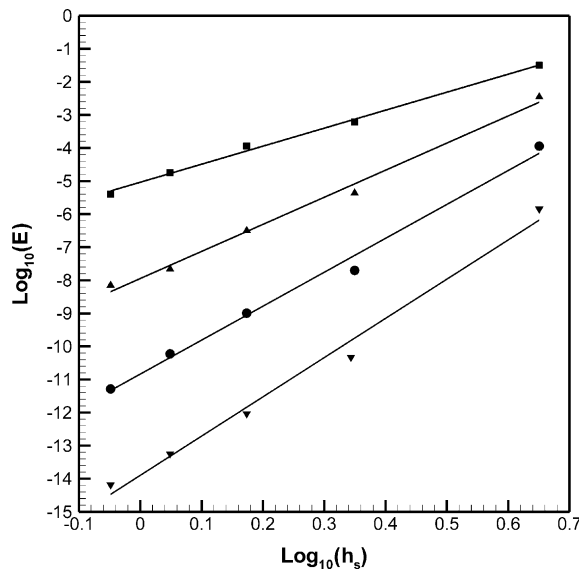

Fig. 8. Convergence plot for the axisymmetric standing wave problem at $t = 1.0$. $E = \frac{d_{N,L^2}(u_N, u_E)}{\|u_E\|_{N,L^2}}$: (■) $N = 5$, (▲) $N = 7$, (●) $N = 9$ and (▼) $N = 11$. Continuous lines: least squares linear approximations.

method for this numerical example. Full second-order accuracy has been achieved, while the reported modifications at the end of subsection 4.1 have succeeded in enabling the Newmark method to handle partial differential equations with first-order pole singularities in their spatial differential operators. Table 13 presents the relative errors with respect to the H^1 norm, for numerical solutions obtained with the explicit temporal approximation method, by utilizing different time steps and polynomial degrees, but for the same geometric configuration and total integration time. Since the Runge–Kutta–Nyström method is only conditionally stable, there exists a maximum allowable time step for every spatial resolution, which can guarantee a bounded numerical solution according to the CFL stability criterion. These critical time step intervals, for the specific numerical simulations conducted, are depicted in Table 13 (where the infinity symbol is employed to denote the occurrence of instability) and decrease with polynomial order as predicted by standard theoretical arguments.

Before ending, it is rather crucial to note that at this test case as well as at both the previous ones, the replacement of the Dirichlet boundary conditions by relation (8) at the intermediate steps of the Runge–Kutta–Nyström method was found to be completely satisfactory, since there was no numerical evidence whatsoever of order reduction, or of any kind of loss of accuracy whenever the specific temporal discretization method was utilized. Finally, let us report that the collaboration between the influence matrix
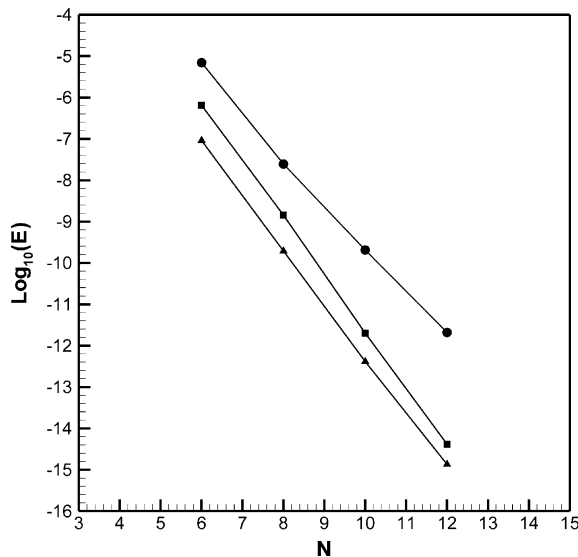

Fig. 9. Convergence plot for the axisymmetric standing wave problem at $t = 0.2$. Complex subdomain topology ($\blacksquare$) $E = \frac{d_{N,L^\infty}(u_N, u_E)}{\|u_E\|_{N,L^\infty}}$, ($\blacktriangle$) $E = \frac{d_{N,L^2}(u_N, u_E)}{\|u_E\|_{N,L^2}}$ and ($\bullet$) $E = \frac{d_{N,H^1}(u_N, u_E)}{\|u_E\|_{N,H^1}}$.

Table 12
Temporal accuracy results for the axisymmetric standing wave problem at $t = 0.2$ (complex subdomain topology and Newmark method)

Δt	$d_{N,L^\infty}(u_N, u_E)/\|u_E\|_{N,L^\infty}$	$d_{N,L^2}(u_N, u_E)/\|u_E\|_{N,L^2}$	$d_{N,H^1}(u_N, u_E)/\|u_E\|_{N,H^1}$
10^{-1}	2.18×10^{-5}	1.30×10^{-5}	1.04×10^{-4}
10^{-2}	3.86×10^{-7}	1.22×10^{-7}	9.92×10^{-7}
10^{-3}	4.52×10^{-9}	1.27×10^{-9}	1.08×10^{-8}
10^{-4}	2.37×10^{-11}	9.65×10^{-12}	1.03×10^{-10}

Table 13
Stability results for the axisymmetric standing wave problem at $t = 0.2$ (complex subdomain topology and Runge–Kutta–Nyström method $E = d_{N,H^1}(u_N, u_E)/\|u_E\|_{N,H^1}$)

Δt	E for $N = 6$	E for $N = 8$	E for $N = 10$	E for $N = 12$
0.0004	1.07×10^{-5}	3.78×10^{-8}	3.15×10^{-10}	3.20×10^{-12}
0.0005	1.07×10^{-5}	3.78×10^{-8}	3.15×10^{-10}	3.20×10^{-12}
0.0008	1.07×10^{-5}	3.78×10^{-8}	3.16×10^{-10}	7.42×10^{-6}
0.0010	1.07×10^{-5}	3.78×10^{-8}	6.16×10^{-10}	$8.85 \times 10^{+1}$
0.0016	1.07×10^{-5}	4.02×10^{-8}	$2.24 \times 10^{+8}$	∞
0.0020	1.07×10^{-5}	5.38×10^{-6}	∞	∞
0.0025	1.07×10^{-5}	$1.33 \times 10^{+3}$	∞	∞
0.0040	9.21×10^{-5}	∞	∞	∞
0.0050	$2.81 \times 10^{+7}$	∞	∞	∞

method and the implicit time integrator, as well as between the LU factorization and the matrix diagonalization methods, were confirmed to perform well and to be quite efficient for subdomain topologies which included a small number of curvilinear elements.

5.4. Wave propagation analysis

Henceforth, we address the issues of dissipation and dispersion errors of the spatial and temporal approximation schemes, along with the resolution requirements necessary for the accurate solution of certain wave propagation problems. We began our numerical simulations by computing two plane wave solutions of the homogeneous acoustic wave equation. The exact solutions were given by the relations:

$$u_E^{Re}(x, y, t) = U_0 \cos(\kappa_x x + \kappa_y y - \omega t),$$

$$u_E^{Im}(x, y, t) = U_0 \sin(\kappa_x x + \kappa_y y - \omega t),$$

with the frequency ω and the Cartesian components κ_x, κ_y of the wave number vector satisfying the dispersion relation $\omega^2 = c_0^2(\kappa_x^2 + \kappa_y^2)$, where c_0 stands for the constant magnitude of the phase velocity of the sinusoidal wavetrains. We used a computational domain of the form $\Omega = (0, L_x) \times (0, L_y)$ and imposed only Dirichlet boundary conditions on the border $\partial\Omega$.

Let us indicate the numerical solutions of the above problems as $u_N^{Re} = u_N^{Re}(x, y, t)$ and $u_N^{Im} = u_N^{Im}(x, y, t)$, respectively. In order to provide a precise definition of the dissipation and dispersion errors, we construct the following complex valued forms of the solutions:

$$u_E^c(x, y, t) = u_E^{Re}(x, y, t) + i u_E^{Im}(x, y, t),$$

$$u_N^c(x, y, t) = u_N^{Re}(x, y, t) + i u_N^{Im}(x, y, t),$$

where $i = \sqrt{-1}$ denotes the imaginary unit. Subsequently, we introduce the ratio of these complex solutions, which in polar form reads:

$$R^c = \frac{u_N^c}{u_E^c} = |R^c| \exp(i \arg R^c),$$

and certainly depends on the spatial and temporal independent variables. The modulus and argument of this complex ratio are scalar functions which take their values in the field of real numbers:

$$|R^c|, \arg R^c : \Omega_I \to \Re.$$

Moreover:

$$|R^c|(t), \arg R^c(t) : I \to X(\Omega),$$

with X a B-space defined over Ω. We set the dissipation (or amplitude) error of the numerical solution in the metric of the space X, to be the time-dependent function:

$$E_X^a = d_{N,X}(|R^c|, 1).$$

Similarly, the dispersion (or phase) error is fixed by the relation:

$$E_X^p = d_{N,X}(\arg R^c, 0).$$

With these definitions at hand, we may proceed with the details of the specific simulations. We used the values $U_0 = 1$, $L_x = L_y = 1$ and $c_0 = \frac{\sqrt{2}}{2}$, while the frequency and the components of the wave number vector assumed the form: $\omega = \kappa_x = \kappa_y = 2\pi/\delta$, with $\delta \in \mathfrak{R}$. We chose $\delta = 0.4$ and set the total integration time as $T = 1$. The computational domain was decomposed into two different subdomain topologies. A nine square element partition was at first considered, and then an unstructured subdomain configuration was employed, similar to the one displayed in Fig. 2, but linearly transformed so as to result with $0 \leqslant x \leqslant L_x$ and $0 \leqslant y \leqslant L_y$. The convergence of the dissipation and dispersion errors of the multidomain weak pseudospectral approximation was exponential, as depicted in Fig. 10. Both the subdomain topologies delivered spectrally convergent results, although the unstructured partition was characterized by higher error levels and slightly smaller asymptotic rates of geometric convergence (see [3]). Tables 14 and 15 present the temporal behavior of the different time integrators, for the nine element configuration. Double precision accuracy was finally achieved by the Runge–Kutta–Nyström method, while the conventional and modified formulations of the Newmark scheme, which produced identical results for the time steps considered, managed to deliver second-order accurate results. The performance of the temporal approximation schemes was quite satisfactory, considering the fact that these methods are not optimized to reach minimum amplitude and phase errors (see [26,27]). Generally, the time step must be limited by the tolerable values of these errors, for time accurate numerical solutions to be obtained.
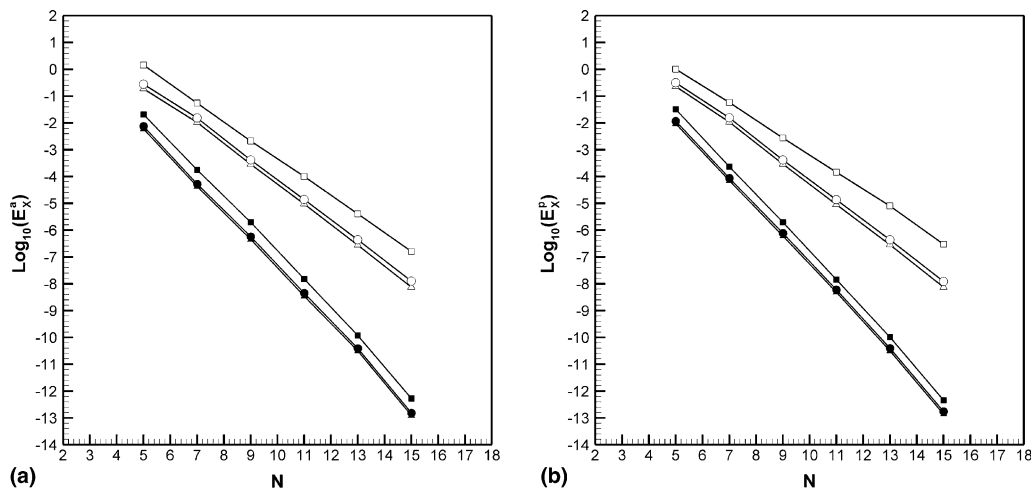

Fig. 10. (a) Dissipation and (b) dispersion errors for the two-dimensional traveling wave problem at $t = 1.0$. Nine subdomain topology: ($\blacksquare$) $X = L^\infty$, ($\blacktriangle$) $X = L^1$ and ($\bullet$) $X = L^2$. Unstructured subdomain topology: ($\square$) $X = L^\infty$, ($\triangle$) $X = L^1$ and ($\circ$) $X = L^2$.

Table 14
Temporal dissipation and dispersion errors for the two-dimensional traveling wave problem at $t = 1.0$ (nine subdomain topology and Runge–Kutta–Nyström method)

Δt	$E_{L^\infty}^a$	$E_{L^1}^a$	$E_{L^2}^a$	$E_{L^\infty}^p$	$E_{L^1}^p$	$E_{L^2}^p$
10^{-2}	5.50×10^{-5}	6.75×10^{-6}	1.09×10^{-5}	8.89×10^{-5}	1.86×10^{-5}	2.34×10^{-5}
10^{-3}	6.27×10^{-9}	4.42×10^{-10}	1.07×10^{-9}	9.58×10^{-9}	1.74×10^{-9}	2.26×10^{-9}
10^{-4}	5.60×10^{-13}	6.53×10^{-14}	1.01×10^{-13}	8.99×10^{-13}	1.57×10^{-13}	2.04×10^{-13}

Table 15
Temporal dissipation and dispersion errors for the two-dimensional traveling wave problem at $t = 1.0$ (nine subdomain topology and Newmark method)

Δt	$E_{L^\infty}^a$	$E_{L^1}^a$	$E_{L^2}^a$	$E_{L^\infty}^p$	$E_{L^1}^p$	$E_{L^2}^p$
10^{-2}	6.80×10^{-2}	6.73×10^{-3}	1.14×10^{-2}	9.16×10^{-2}	1.86×10^{-2}	2.41×10^{-2}
10^{-3}	7.01×10^{-4}	6.60×10^{-5}	1.15×10^{-4}	1.03×10^{-3}	1.86×10^{-4}	2.42×10^{-4}
10^{-4}	6.87×10^{-6}	6.62×10^{-7}	1.15×10^{-6}	1.08×10^{-5}	1.86×10^{-6}	2.42×10^{-6}

Next, we continue with the wavelength and period resolution requirements of the different numerical methodologies. It is fairly common (see [1]) for the resolution of a spectral spatial discretization procedure, to be represented by the polynomials (or modes) per wavelength, necessary for the method to adequately resolve the oscillating structure of a given wave, within some level of a priori prescribed error tolerance. The same argument applies to the time integration schemes, only now one is interested to know the number of points (or discrete time instants) per period, capable of capturing the distinctive features of the wave's temporal evolution. Before proceeding with the detailed exposition of the results, the following definitions are in order. Suppose we are solving for a two-dimensional sinusoidal wavetrain, with Cartesian wave number vector components κ_x, κ_y and frequency ω, in a computational domain of the form $\Omega = (0, L_x) \times (0, L_y)$. In order to be conservative with our estimations of the resolution capabilities of the spatial discretization scheme, let us set the number of wavelengths contained in Ω as:

$$N_w = \begin{cases} \frac{L_x \kappa_x}{2\pi}, & \kappa_x \neq 0, \quad \kappa_y = 0, \\ \frac{L_y \kappa_y}{2\pi}, & \kappa_x = 0, \quad \kappa_y \neq 0, \\ \min\left\{ \frac{L_x \kappa_x}{2\pi}, \frac{L_y \kappa_y}{2\pi} \right\}, & \kappa_x \kappa_y \neq 0. \end{cases}$$

It is relatively straightforward to represent the number of modes per wavelength and element, employed by the spatial approximation method, as the ratio N/N_w. The temporal period T_p of the wave motion is defined, at any fixed spatial position, as the shortest time interval between two successive appearances of the same phase, namely $T_p = 2\pi/\omega$. Consequently, the points per period utilized by the time integrator, are given by $T_p/\Delta t$.

Towards the quantification of the above resolution parameters, we concerned ourselves with the numerical solution of the homogeneous two-dimensional acoustic wave equation, for the real part of the analytical complex valued wavefunction previously considered. The mathematical setting of the problem was retained along with all the simulation parameters, apart from δ which assumed the values 0.1 and 0.2, and from the final time for the computations which was fixed as $T = \delta$. We also considered different domain decompositions than before, in particular a one domain configuration, a four and a nine square subdomain partition. It is obvious that for the specific calculations $N_w = 1/\delta$, and that the temporal period of the wave motion was identified with δ. Fig. 11 displays the results of the spatial convergence for the spectral approximation with respect to the ratio N/N_w. From this diagram, we can roughly conclude that to achieve 1% accuracy for a wave-like solution, one needs 3.6, 2.0 and 1.4 polynomials per wavelength and subdomain,

for the one, four and nine element decompositions, respectively. The result concerning the monodomain topology, is in agreement with the one presented by Gottlieb and Orszag in [1], as well as by Boyd in [3] for the one-dimensional case. It appears that the spatial approximation method (and particularly its multi-domain version) is quite effective for the resolution of wave phenomena, especially in comparison with finite difference and low order finite element discretizations. Error results for the time integration procedures with respect to the number of time steps per period, are presented in Tables 16 and 17 for the nine subdomain topology. In a similar manner, we can reach the conclusion that in order to resolve the temporal evolution of a wave-like function within 1% of accuracy in the L^2 norm, one should use approximately 10.8 points per period with the Runge–Kutta–Nyström method and 37.5 points per period with the Newmark time integration scheme. This behavior is typical emanating from fourth- and second-order accurate discretization methods, respectively.
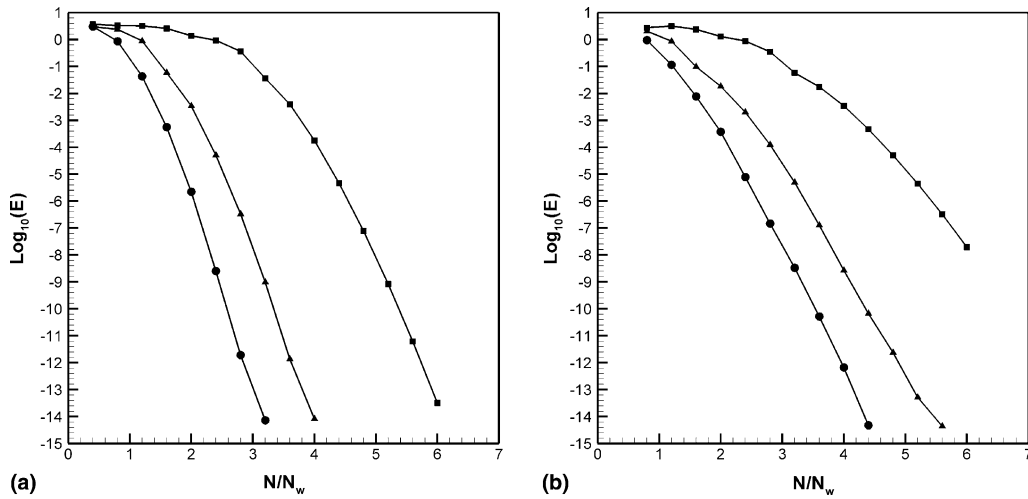

Fig. 11. Convergence plot for the two-dimensional traveling wave problem at $t = 1.0$ for: (a) $\delta = 0.1$ and (b) $\delta = 0.2$. $E = d_{N,L^2}(u_N, u_E)$: (■) monodomain topology, (▲) four subdomain topology and (●) nine subdomain topology.

Table 16
Temporal resolution results for the two-dimensional traveling wave problem (nine subdomain topology and Runge–Kutta–Nyström method)

δ	$T_p/\Delta t$	$d_{N,L^\infty}(u_N, u_E)$	$d_{N,L^2}(u_N, u_E)$	$d_{N,H^1}(u_N, u_E)$
0.1	10	7.82×10^{-1}	4.12×10^{-2}	9.63×10^{0}
	20	1.23×10^{-2}	2.21×10^{-4}	7.16×10^{-2}
	40	1.79×10^{-5}	8.35×10^{-6}	7.81×10^{-4}
	80	1.13×10^{-6}	5.19×10^{-7}	4.84×10^{-5}
	160	7.04×10^{-8}	3.25×10^{-8}	2.93×10^{-6}
0.2	10	3.25×10^{-2}	7.42×10^{-3}	8.16×10^{-1}
	20	4.42×10^{-4}	1.50×10^{-4}	1.25×10^{-2}
	40	1.77×10^{-5}	8.19×10^{-6}	3.82×10^{-4}
	80	1.16×10^{-6}	5.10×10^{-7}	2.34×10^{-5}
	160	7.23×10^{-8}	3.18×10^{-8}	1.46×10^{-6}

Table 17
Temporal resolution results for the two-dimensional traveling wave problem (nine subdomain topology and Newmark method)

δ	$T_p/\Delta t$	$d_{N,L^\infty}(u_N, u_E)$	$d_{N,L^2}(u_N, u_E)$	$d_{N,H^1}(u_N, u_E)$
0.1	20	7.40×10^{-2}	3.52×10^{-2}	3.15×10^{0}
	40	1.88×10^{-2}	8.89×10^{-3}	7.97×10^{-1}
	80	4.71×10^{-3}	2.23×10^{-3}	2.00×10^{-1}
	160	1.18×10^{-3}	5.58×10^{-4}	4.99×10^{-2}
	320	2.95×10^{-4}	1.39×10^{-4}	1.25×10^{-2}
	640	7.37×10^{-5}	3.49×10^{-5}	3.12×10^{-3}
0.2	20	7.46×10^{-2}	3.43×10^{-2}	1.55×10^{0}
	40	1.89×10^{-2}	8.66×10^{-3}	3.91×10^{-1}
	80	4.75×10^{-3}	2.17×10^{-3}	9.80×10^{-2}
	160	1.19×10^{-3}	5.43×10^{-4}	2.45×10^{-2}
	320	2.96×10^{-4}	1.36×10^{-4}	6.13×10^{-3}
	640	7.41×10^{-5}	3.39×10^{-5}	1.53×10^{-3}

The numerical simulations in this subsection confirmed the excellent convergence properties of the approximation methods, as far as the dissipation and dispersion errors are concerned. The spatial discretization scheme succeeded in delivering exponentially convergent amplitude and phase errors, regardless of the unstructured topology of the domain decomposition, while the temporal integrators behaved satisfactorily in wave propagation computations, despite the fact that they are not optimized for a usage of this kind.

5.5. Absorbing boundary conditions and dissipative wave equations

We proceeded by testing the ability of the numerical schemes to handle Robin boundary conditions, as well as more general hyperbolic differential operators. Towards this end, we utilized test cases similar to the ones presented in [28], which concerned the evolution of Gaussian pulses in computational domains with absorbing boundaries. In this context, we considered the following initial boundary value problem:

$$\left\|\begin{aligned} &\frac{\partial^2 u}{\partial t^2} - c_0^2 \left(\frac{\partial^2 u}{\partial x^2} + \frac{\partial^2 u}{\partial y^2} \right) = 0 \quad \text{on } \Omega_I, \\ &u = \exp\{-a_p[(x - x_0)^2 + (y - y_0)^2]\} \quad \text{on } \Omega \text{ for } t = 0, \\ &\frac{\partial u}{\partial t} = 0 \quad \text{on } \Omega \text{ for } t = 0, \\ &\frac{\partial u}{\partial n_L} + c_0 \frac{\partial u}{\partial t} + \frac{c_0^2 \kappa}{2} u = 0 \quad \text{on } \Gamma_R \times I, \end{aligned}\right.$$

with $a_p, x_0, y_0 \in \Re$, $\Gamma_R = \partial \Omega$ and $\kappa : \Gamma_R \to \Re$ the curvature of the Robin portion of the boundary. Suppose that an open subset $\Gamma \subseteq \Gamma_R$ is defined by the set of equations $x = x(\varsigma)$, $y = y(\varsigma)$ with $x, y : \Sigma \subset \Re \to \Re$ and $x, y \in C^2(\Sigma)$. Then the curvature of Γ is defined on any of its points as the function:

$$\kappa(\varsigma) = \frac{\left| \frac{dx}{d\varsigma} \frac{d^2 y}{d\varsigma^2} - \frac{dy}{d\varsigma} \frac{d^2 x}{d\varsigma^2} \right|}{\left\{ \left(\frac{dx}{d\varsigma} \right)^2 + \left(\frac{dy}{d\varsigma} \right)^2 \right\}^{3/2}}.$$

The Robin boundary condition which was imposed, belongs to the family of first-order radiation boundary conditions (see [29–33]) which allow disturbances to exit the computational field and let us use finite domains for the simulation of unbounded wave propagation. An elegant method to evaluate the performance of an absorbing boundary condition, as well as to confirm its correct numerical implementation, is to

calculate the evolution of the total energy of the wave field over the physical portion of the computational domain. We use the term "physical domain" to denote the subset $\Omega_p \subseteq \Omega$ on which we are interested in accurately simulating wave propagation with minimum dispersion and dissipation errors, in contradiction with the "sponge domain" to be defined later in this subsection. The total energy over Ω_p is defined to be:

$$e = \frac{1}{2} \int_{\Omega_p} \int \left\{ \left(\frac{\partial u}{\partial x}\right)^2 + \left(\frac{\partial u}{\partial y}\right)^2 + \frac{1}{c_0^2} \left(\frac{\partial u}{\partial t}\right)^2 \right\},$$

and certainly is a function of time. For the discrete evaluation of the above form, we fix the set of subdomain indices $M_p = \{m \in M | \Omega^m \subseteq \Omega_p\} \subseteq M$ and specify:

$$e_N = \frac{1}{2} \sum_{m \in M_p} \sum_{\vec{i} \in J} \left\{ \left(\left\langle \frac{\partial u_N^m}{\partial x} \right\rangle_{\vec{i}}\right)^2 + \left(\left\langle \frac{\partial u_N^m}{\partial y} \right\rangle_{\vec{i}}\right)^2 + \frac{1}{c_0^2} \left(\left\langle \frac{\partial u_N^m}{\partial t} \right\rangle_{\vec{i}}\right)^2 \right\} \langle |J_N^m| \rangle_{\vec{i}} \, \omega_{\vec{i}},$$

with $u_N^m(t) : I \to C^1(\bar{D})$ and $\frac{\partial u_N^m}{\partial t}(t) : I \to C^0(\bar{D})$, for $m \in M$. Please notice that the computation of the discrete energy at any time level is straightforward, since both the Newmark as well as the Runge–Kutta–Nyström time integration algorithms store the values of the first-order temporal derivative of the wave variable at all the grid nodes of the computational domain.

For the first part of our numerical experiments, we considered the rectangular domain $\Omega = \Omega_p = (0,1)^2$ which we subdivided into four subdomains of equal size. We used $c_0 = 2$, $a_p = 500$ and performed numerical simulations with Gaussian pulses initiated at the centre of the domain $(x_0, y_0) = (0.5, 0.5)$, as well as at the point $(x_0, y_0) = (0.1, 0.1)$ which is located near the corner. We utilized the Newmark method for our simulations with $\Delta t = 0.0004$ and set the degree of the polynomial approximation as $N = 25$. The open time domains that we considered were $I = (0.0, 0.4)$ and $I = (0.0, 0.8)$ for the computations with the initial pulse located at the centre and near the corner of the physical domain, respectively. The evolution of the discrete total energy divided by the energy of the wave field at the initial time $e_{N,0} = e_N(0)$ is presented in Fig. 12 for these two simulations. Gradual decay of the wave energy is observed as the pulse exits the computational domain, which confirms the success of the radiation boundary condition, as well as its correct numerical enforcement by the weak collocation method.

Next, we proceeded with a different computational domain, namely $\Omega = \Omega_p = D[(0.5, 0.5), 1.0]$, where $D(C_0, R_0)$ is used to denote the disk of radius R_0 with its centre at C_0, endowed with the subdomain topol-
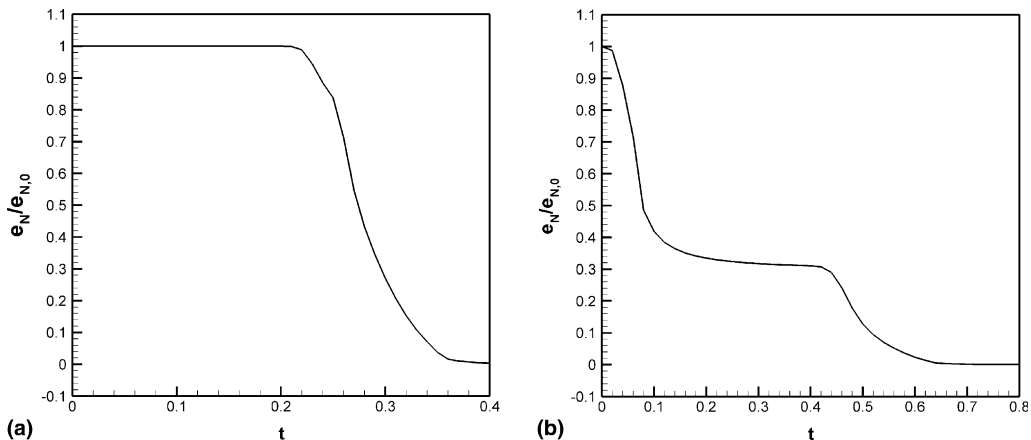

Fig. 12. Temporal evolution of the scaled discrete total energy for a pulse initially located at (a) $(x_0, y_0) = (0.5, 0.5)$ and (b) $(x_0, y_0) = (0.1, 0.1)$. Rectangular computational domain. Absorbing boundary conditions.

ogy shown in Fig. 13. For this test case, we utilized the Runge–Kutta–Nyström method for the temporal integration with $\Delta t = 0.002$, along with $a_p = 50$ and a polynomial degree $N = 10$ for the pseudospectral method. The wave speed and the initial pulse locations were kept the same as previously, but we used $T = 0.8$ and $T = 1.6$ as the final times for our computations of the pulses initially placed at the centre and near the boundary of the physical domain, respectively. The scaled discrete total energy is depicted in Fig. 14, where a similar decay as in the case of the rectangular domain is observed, which leads us to conclude the ability of the absorbing boundary condition to handle domains with curved boundaries, along with the success of the spectral method in enforcing Robin boundary operators on curvilinear borders.
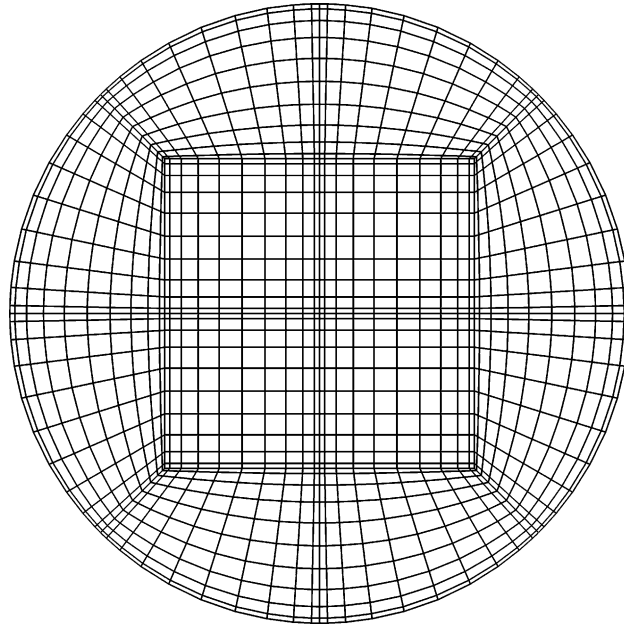

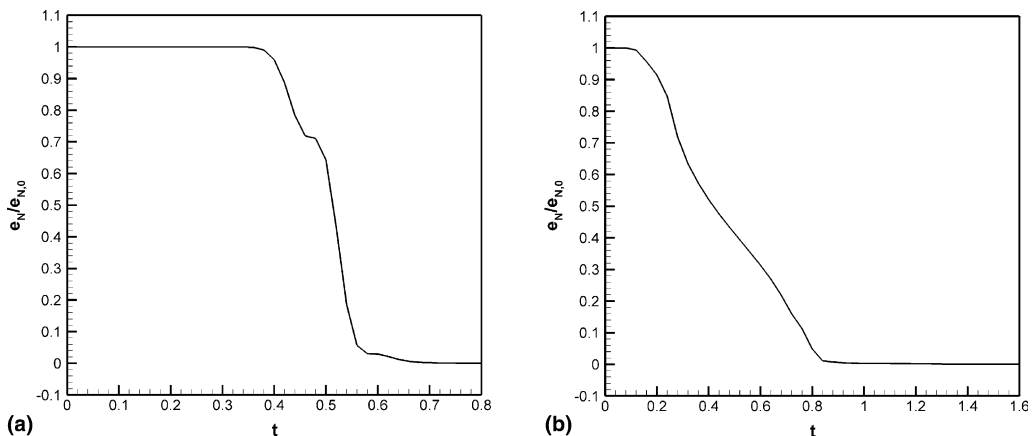Fig. 13. Unstructured grid with $N = 10$, for the disk computational domain.

Fig. 14. Temporal evolution of the scaled discrete total energy for a pulse initially located at (a) $(x_0, y_0) = (0.5, 0.5)$ and (b) $(x_0, y_0) = (0.1, 0.1)$. Disk computational domain. Absorbing boundary conditions.

Subsequently, we validated the proposed numerical methodologies in the framework of dissipative wave differential operators. Towards this, we considered the following initial boundary value problem:

$$\left\| \begin{array}{l} \frac{\partial^2 u}{\partial t^2} + d_a \sigma \frac{\partial u}{\partial t} - c_0^2 \left(\frac{\partial^2 u}{\partial x^2} + \frac{\partial^2 u}{\partial y^2} \right) + d_b \sigma^2 u = 0 \quad \text{on } \Omega_I, \\ u = \exp\{-a_p[(x - x_0)^2 + (y - y_0)^2]\} \quad \text{on } \Omega \text{ for } t = 0, \\ \frac{\partial u}{\partial t} = 0 \quad \text{on } \Omega \text{ for } t = 0, \\ u = 0 \quad \text{on } \Gamma_D \times I, \end{array} \right.$$

with $d_a, d_b \in \Re$, $\Gamma_D = \partial \Omega$ and $\sigma : \Omega \to \Re$. Let us comment for a while on the specific form of the function $\sigma = \sigma(x,y)$. Consider a subset $\Omega_s \subset \Omega$ such that $\bar{\Omega}_s \cup \bar{\Omega}_p = \bar{\Omega}$ and $\Omega_s \cap \Omega_p = \emptyset$. Ω_s is called "sponge domain" (or "damping zone", or "absorbing layer") and its closure comprises the support of the sponge function σ. More precisely, $\sigma \geqslant 0$ on $\bar{\Omega}_s$ and $\sigma = 0$ identically on $\bar{\Omega}_p$, with $\sigma \in C^0(\bar{\Omega})$. In this way, we ensure that the wave disturbances that propagate inside the sponge region are progressively attenuated, while they are left unaffected inside the physical portion of the computational domain. The specific shape of the damping zone, along with the precise form of the sponge function, determines the dissipative properties of the absorbing layer. M_s is defined to be the subset of indices of the subdomains that belong to the sponge zone, namely $M_s = \{m \in M | \Omega^m \subseteq \Omega_s\} \subset M$ and we assume that the subdomain decomposition is such that $M_p \cup M_s = M$ and $M_p \cap M_s = \emptyset$. In our simulations, the restrictions of the sponge function in each subdomain read, in the local coordinate system $(r,s) \in \bar{D}^2$:

$$\sigma^m(r,s) = \begin{cases} \sigma_M \left[\sigma_r^m \left(\frac{1 + \sigma_a^m r}{2} \right)^{\sigma_e} + \sigma_s^m \left(\frac{1 + \sigma_b^m s}{2} \right)^{\sigma_e} \right], & m \in M_s, \\ 0, m \in M_p, \end{cases}$$

with $\sigma_r^m, \sigma_s^m = 0$ or 1 and $\sigma_a^m, \sigma_b^m = 1$ or -1 being the parameters which determine the specific form of the sponge function in accordance to the position of $\Omega^m \subseteq \Omega_s$ relatively to the physical domain and to the computational border so that at the end σ to be globally continuous, and $\sigma_M, \sigma_e \in \Re$ being parameters defined by the user in order to control the shape of the sponge function as well as its damping capabilities.

In all our numerical experiments, we utilized the rectangular physical domain $\Omega_p = (0,1)^2$. First, we considered the computational domain $\Omega = (-0.5, 1.5)^2$ partitioned into 16 equally sized elements and used the Newmark method for the temporal discretization with $\Delta t = 0.0004$. Let us say that here as well as in the previous studies where we utilized absorbing boundary conditions, we ensured that the difference between the classical and the modified implementations of the Newmark method gave graphically indistinguishable results for the time steps used. Also note that we were allowed to apply the matrix diagonalization method for the direct solution of the discrete linear system of equations in a specific orthogonal subdomain Ω^m whenever $d_b \sigma_r^m \sigma_s^m = 0$ with the implicit Newmark method, a fact that made the overall algorithm even more efficient. We used a polynomial degree of $N = 25$ and utilized the values $c_0 = 2$, $\sigma_M = 40$ and $a_p = 500$. Like in the case with the absorbing boundary conditions, we conducted simulations with Gaussian pulses initiated at the points $(x_0, y_0) = (0.5, 0.5)$ and $(x_0, y_0) = (0.1, 0.1)$ and accordingly used two time intervals defined as $I = (0,1)$ and $I = (0.0, 1.6)$. Fig. 15 shows the decay of the discrete total energy of the wave field for different sets of parameters d_a, d_b and σ_e, for the case of the initial pulse located at the centre of the physical domain. It is rather interesting to observe that the choice $(d_a, d_b) = (2,1)$ in the partial differential equation leads to the formulation proposed by Kosloff and Kosloff in [34], while when $(d_a, d_b) = (1,0)$ we have the "Newtonian cooling" or "friction" effect described by Israeli and Orszag in [35]. Similarly, the scaled discrete total energy for the initially located pulse near the corner of the physical region, is illustrated in Fig. 16. Note that in the case when $\sigma_e = 2$, the results for the temporal evolution of the scaled total energy are graphically indistinguishable between the two choices of the parameters d_a and d_b, for both the locations of the initial pulses. Furthermore, noticeable partial wave reflection is observed whenever $\sigma_e = 10$, since in this
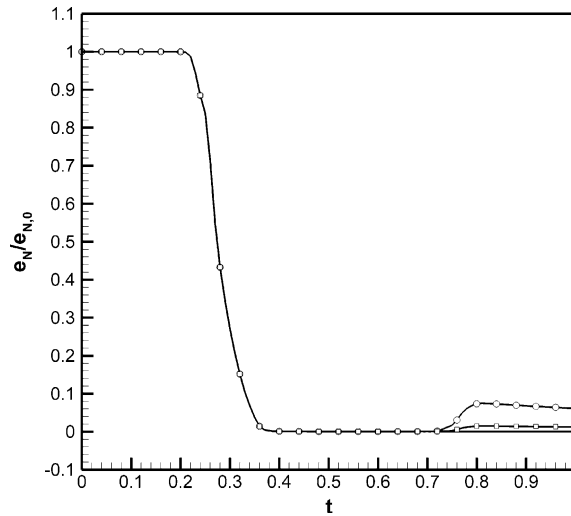
Fig. 15. Temporal evolution of the scaled discrete total energy for a pulse initially located at $(x_0, y_0) = (0.5, 0.5)$. Rectangular computational domain. Dissipative wave equations. Dashed line: $\sigma_e = 2$ and $(d_a, d_b) = (1, 0)$. Continuous line: $\sigma_e = 2$ and $(d_a, d_b) = (2, 1)$. Continuous line with circles: $\sigma_e = 10$ and $(d_a, d_b) = (1, 0)$. Continuous line with squares: $\sigma_e = 10$ and $(d_a, d_b) = (2, 1)$.
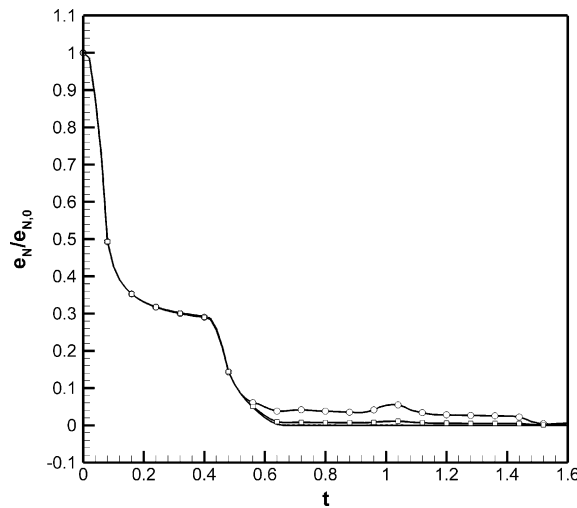

Fig. 16. Temporal evolution of the scaled discrete total energy for a pulse initially located at $(x_0, y_0) = (0.1, 0.1)$. Rectangular computational domain. Dissipative wave equations. Dashed line: $\sigma_e = 2$ and $(d_a, d_b) = (1, 0)$. Continuous line: $\sigma_e = 2$ and $(d_a, d_b) = (2, 1)$. Continuous line with circles: $\sigma_e = 10$ and $(d_a, d_b) = (1, 0)$. Continuous line with squares: $\sigma_e = 10$ and $(d_a, d_b) = (2, 1)$.

occasion the damping varies more rapidly than the wave itself (see [3]). This is the appropriate time to state that we did not, by any means, attempt to conduct a parametric study so as to determine the optimum choice of parameters for best dissipative effects in the damping zone, but rather performed these simulations in order to provide numerical evidence that the proposed methods face no difficulty in solving more general wave equations with first-order temporal differential operators.

Finally, we ended this series of test cases by employing the Newmark method for the solution of the same problem on the disk $\Omega = D[(0.5, 0.5), 1.0]$ with the subdomain topology displayed in Fig. 13. This time, the

physical domain retained its form but the values $N = 10$, $\Delta t = 0.002$, $a_p = 50$ and $T = 1$ were used for studying the temporal evolution of a Gaussian pulse originated at the centre of the computational domain. Plots of the dependence of the scaled discrete total energy of the wave variable on time are presented on Fig. 17 for two different choices of the parameters which determine the nature of the absorbing zone. The derived results have the predictable decreasing trend and confirm the ability of our numerical method to accurately simulate dissipative wave phenomena in curvilinear coordinates.

Before ending, let us mention that the overall conclusions we drew from the numerical experiments of this subsection are the capability of the combined spatial and temporal approximation methods of incorporating Robin boundary operators on straight and curved boundaries, as well as the accurate solution of different forms of dissipative wave equations on general subdomain topologies.

5.6. Acoustic pressure pulse evolution in an axisymmetric constricted tube

In this last problem, we faced a situation more oriented towards applications, namely the axisymmetric propagation of an acoustic pressure pulse inside a pipe presenting a cosine stenosis. The totality of aeroacoustic processes in axisymmetric inviscid fluid flows are governed by the Euler differential equations for compressible fluids, which in an appropriate nondimensional form, read:

$$\frac{\partial \vec{Q}}{\partial t} + \frac{\partial \vec{F}_x}{\partial x} + \frac{\partial \vec{F}_y}{\partial y} = \vec{S},$$

where:

$$\vec{Q} = \begin{bmatrix} \rho \\ \rho u_x \\ \rho u_y \\ \rho E_t \end{bmatrix}, \quad \vec{F}_x = \begin{bmatrix} \rho u_x \\ p + \rho u_x^2 \\ \rho u_x u_y \\ \rho u_x H_t \end{bmatrix}, \quad \vec{F}_y = \begin{bmatrix} \rho u_y \\ \rho u_x u_y \\ p + \rho u_y^2 \\ \rho u_y H_t \end{bmatrix} \quad \text{and} \quad \vec{S} = -\frac{1}{y} \begin{bmatrix} \rho u_y \\ \rho u_x u_y \\ \rho u_y^2 \\ \rho u_y H_t \end{bmatrix},$$
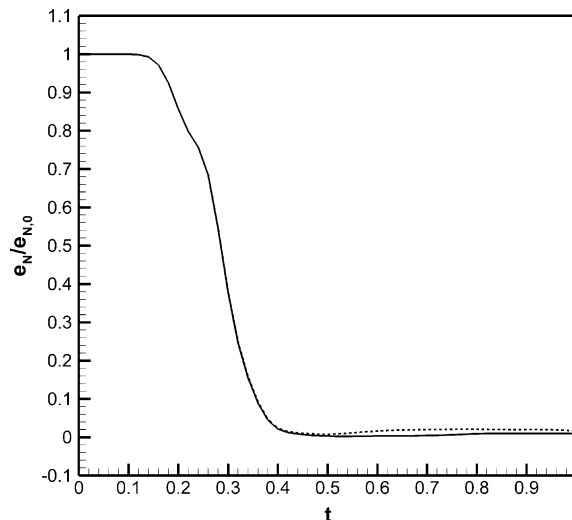

Fig. 17. Temporal evolution of the scaled discrete total energy for a pulse initially located at $(x_0, y_0) = (0.5, 0.5)$. Disk computational domain. Dissipative wave equations. Continuous line: $\sigma_e = 2$ and $(d_a, d_b) = (1, 0)$. Dashed line: $\sigma_e = 2$ and $(d_a, d_b) = (2, 1)$.

with ρ, u_x, u_y and p the nondimensional depended variables of density, axial velocity, radial velocity and pressure, respectively, while (x, y) are interpreted as the axial and radial coordinates in a cylindrical frame of reference. The variables of total energy and total enthalpy per unit mass are defined to be:

$$E_t = \frac{p}{(\gamma_g - 1)\rho} + \frac{u_x^2 + u_y^2}{2} \quad \text{and} \quad H_t = E_t + \frac{p}{\rho},$$

with γ_g the specific heat ratio. Since we are concerned with the evolution of small amplitude disturbances in a stationary fluid medium, we may write that:

$$\rho = \rho_0 + \rho', \quad u_x = u_x', \quad u_y = u_y' \quad \text{and} \quad p = p_0 + p',$$

where the constants $\rho_0, p_0 \in \Re$ with $\rho_0, p_0 > 0$ are of the order of unity, while the perturbations ρ', u_x', u_y' and p' are functions of the spatial and temporal independent variables such that $\|\rho'\|_{L^\infty} \ll \rho_0, \|u_x'\|_{L^\infty} \ll 1, \|u_y'\|_{L^\infty} \ll 1$ and $\|p'\|_{L^\infty} \ll p_0$ for all times. Then, by the usage of standard linearization techniques we reach the conclusion that the temporal evolution of the pressure field p', is governed by the axisymmetric acoustic wave equation with constant wave speed defined by the relation $c_0^2 = \gamma_g \frac{p_0}{\rho_0}$.

In view of this fact, we considered the numerical solution of the following initial boundary value problem:

$$\left\| \begin{array}{l} \frac{\partial^2 p'}{\partial t^2} - c_0^2 \left(\frac{\partial^2 p'}{\partial x^2} + \frac{\partial^2 p'}{\partial y^2} + \frac{1}{y} \frac{\partial p'}{\partial y} \right) = 0 \quad \text{on } \Omega_I, \\ p' = \varepsilon \exp\{-a_p[(x - x_0)^2 + (y - y_0)^2]\} \quad \text{on } \Omega \text{ for } t = 0, \\ \frac{\partial p'}{\partial t} = 0 \quad \text{on } \Omega \text{ for } t = 0, \\ \frac{\partial p'}{\partial n_L} = 0 \quad \text{on } \Gamma_N \times I, \\ \frac{\partial p'}{\partial n_L} + c_0 \frac{\partial p'}{\partial t} + \frac{c_0^2 \kappa}{2} p' = 0 \quad \text{on } \Gamma_R \times I, \end{array} \right.$$

with $\varepsilon, a_p, x_0, y_0 \in \Re$ and κ the curvature of the Robin portion of the computational boundary. The spatial domain was bounded by:

$$\Gamma_N = \{(x, y) \in \partial\Omega \,|\, (x, y) \in C_w\} \cup \{(x, y) \in \partial\Omega \,|\, x \in (-L_x, L_x), y = 0\},$$

$$\Gamma_R = \{(x, y) \in \partial\Omega \,|\, x = -L_x, y \in (0, L_y)\} \cup \{(x, y) \in \partial\Omega \,|\, x = L_x, y \in (0, L_y)\},$$

with the curve C_w defined as:

$$C_w : y = \begin{cases} L_y, & -L_x \leqslant x < -L_c, \\ L_y - \frac{a_c}{2} L_y \left\{ 1 - \cos\left[\pi \left(1 - \frac{x}{L_c} \right) \right] \right\}, & -L_c \leqslant x \leqslant L_c, \\ L_y, & L_c < x \leqslant L_x, \end{cases}$$

where $a_c, L_x, L_y, L_c \in \Re$.

For validation purposes, a solution of the axisymmetric Euler equations was also obtained by utilizing a combination of a spectral collocation form of the discontinuous Galerkin finite element method for the spatial discretization, along with a standard fourth-order Runge–Kutta method for the temporal integration of the resulting system of first-order ordinary differential equations. The discontinuous Galerkin method for hyperbolic systems of conservation laws has been studied in detail in [36,37]. A spectral element implementation has been proposed by Kopriva et al in [38,39] and used in a different context in [40], while several studies have proved the capability of such methods for accurately solving wave propagation problems by utilization of high order polynomial approximation and achievement of small phase and dissipation errors (see [41,42]). In this article, we considered a conforming collocation form of the discontinuous

Galerkin method for the Euler equations (like in [43]), where the solution was approximated by a tensor product Legendre expansion, while the inner products were replaced by Legendre-Gauss quadratures. To obtain a high resolution representation of the underlying geometry, we employed Legendre-Gauss-Lobatto interpolation rules for the spatial variables in combination with isoparametric mapping techniques for the treatment of irregular solution domains. By properly choosing the flux computation points, this methodology only required communication between subdomains which shared common edges, while the difference in the flux values computed from the neighboring elements was resolved by the approximate Riemann solver of Roe [44]. The Euler equations were solved on the same computational domain as the acoustic wave equation, and over the same subdomain topology. The initial conditions utilized, assumed the form:

$$\rho = \rho_0, \quad u_x = 0, \quad u_y = 0, \quad p = p_0 + \varepsilon \exp\{-a_{\mathrm{p}}[(x - x_0)^2 + (y - y_0)^2]\},$$

on Ω for $t = 0$. Reflective boundary conditions were imposed on the upper wall of the tube and on the symmetry axis, while one-dimensional characteristic boundary conditions were enforced on the right and left computational boundaries by setting appropriate external conditions to the Riemann solver.

In our simulations, we used a high resolution mesh and a subdomain configuration comprised by six elements, which is displayed on Fig. 18. The time interval for the computations was chosen to be $I = (0,5)$. For the solution of the acoustic wave equation the Runge–Kutta–Nyström method was employed for the temporal integration. We considered the values $c_0 = 1$, $\varepsilon = 0.0001$, $a_p = 50$, $(x_0,y_0) = (-0.5,0.0)$, $L_x = 2.5$, $L_y = 1.0$, $L_c = 0.5$, $a_c = 0.5$, $\rho_0 = 1$ and $\gamma_{\mathrm{g}} = 1.4$ for our calculations. Each method was employed to perform two simulations, one with $N = 22$ and $\Delta t = 0.0005$, and another with $N = 25$ and $\Delta t = 0.0002$. Almost identical results (within graphical accuracy) were found, so for the sake of brevity we present only the ones produced by the higher resolution simulations. Contour plots of the pressure disturbance field p', as computed by the weak collocation algorithm, are illustrated in Fig. 18 for various time levels. Notice the smoothness of the solution although the spatial approximation method does not ensure the C^1 continuity of the pressure field except in the limit of infinite resolution. The relative differences between the solutions as computed by the two methodologies are displayed in Table 18 for several time levels. The discrete norm and metric functions involved in the computation of these differences were calculated using Legendre-Gauss quadrature formulas. Very good agreement was concluded, taking under consideration that the acoustic wave equation is only a first-order in ε approximation of the Euler equations. The axial distribution of the pressure perturbation variables is illustrated in Fig. 19 for the specific time levels presented in Fig. 18 and in Table 18, as calculated by the two different methods. The results are observed to be graphically indistinguishable, a fact which is confirmed by the amplitude of the relative differences presented in Table 18.

The axisymmetric form of the acoustic wave equation was also solved by the conventional and modified formulations of the Newmark time integration method, utilizing the same spatial and temporal resolutions as previously. The difference between the solutions obtained by the modified and the classical implementations of the Newmark scheme was negligible for the time steps considered. Table 19 displays the relative differences between the Newmark pseudospectral solution of the wave equation and the Runge–Kutta discontinuous Galerkin solution of the Euler equations, for the higher resolution simulations. Direct comparison between Tables 18 and 19 reveals an outstanding agreement among the pressure fields produced by the different temporal approximation methods for the acoustic wave equation.

Subsequently, we concentrated on the efficiency of the numerical schemes with respect to CPU time and computer memory usage. For the thorough examination of the relative performances between the various methods, we formed the ratios:

$$\Lambda_{\mathrm{RKDG},t}^{\mathrm{Me}} = \frac{C_t^{\mathrm{Me}}}{C_t^{\mathrm{RKDG}}} \quad \text{and} \quad \Lambda_{\mathrm{RKDG},m}^{\mathrm{Me}} = \frac{C_m^{\mathrm{Me}}}{C_m^{\mathrm{RKDG}}},$$
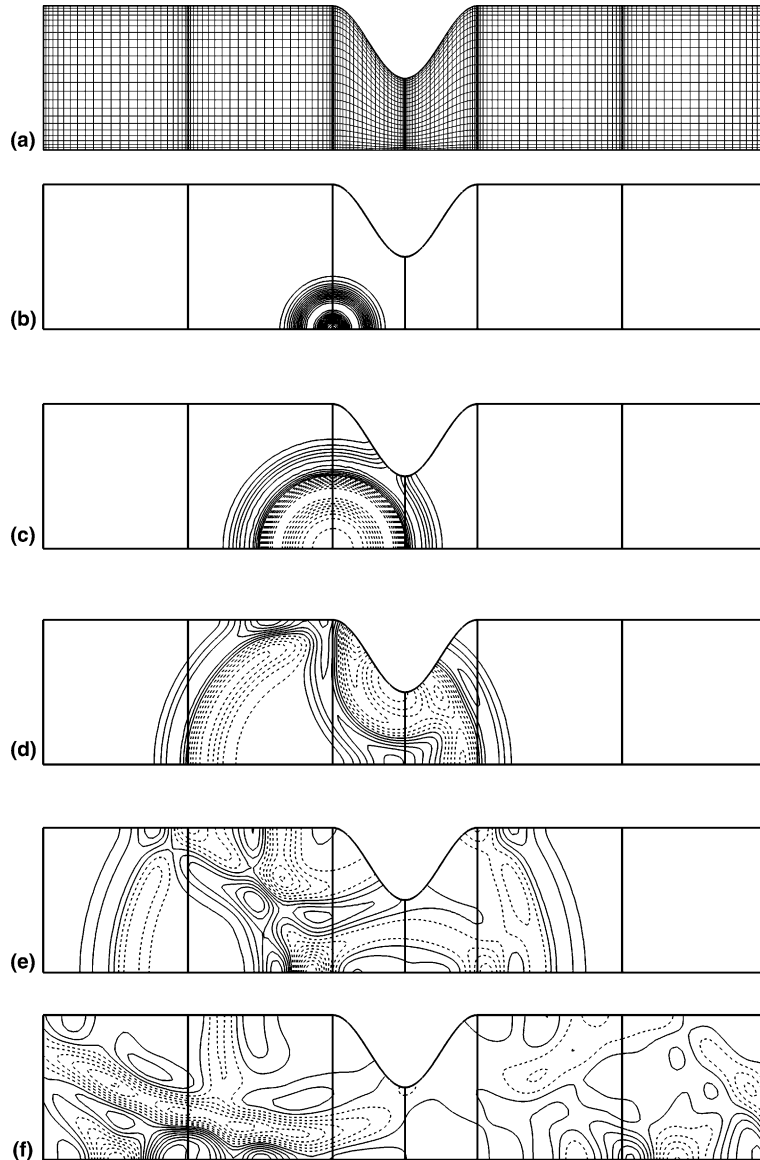
Fig. 18. Axisymmetric constricted tube acoustic simulation: grid (a), and pressure perturbation variable contour plots at (b) $t = 0.1$, (c) $t = 0.5$, (d) $t = 1.0$, (e) $t = 1.5$ and (f) $t = 3.8$ (Dashed lines are used for the negative contours).

where C_t^{Me} and C_m^{Me} are already defined in subsection 5.2 for the multidomain Legendre pseudospectral method, while the symbols C_t^{RKDG} and C_m^{RKDG} are used to indicate analogous quantities for the Runge–Kutta discontinuous Galerkin method. Table 20 presents the performance results for all the numerical algorithms utilized in the proceeding simulations of this subsection. It is worth noticing that the collaboration between the Runge–Kutta–Nyström and the weak Legendre collocation method was the most demanding in terms of CPU time and the least memory consuming. While the latter observation is quite expected, the former, which is seemingly unreasonable, can be explained by the fact that the Runge–Kutta–Nyström method requires computations of second-order spatial partial derivatives on all nodes of the pseudospectral

Table 18
Relative differences of the pressure perturbation variable as calculated by the Runge–Kutta–Nyström Legendre pseudospectral and the Runge–Kutta discontinuous Galerkin methods for the acoustic pulse evolution inside an axisymmetric constricted tube

t	$d_{\mathrm{N},L^\infty}(p'_{ps}, p'_{dg})/\|p'_{dg}\|_{\mathrm{N},L^\infty}$	$d_{\mathrm{N},L^2}(p'_{ps}, p'_{dg})/\|p'_{dg}\|_{\mathrm{N},L^2}$	$d_{\mathrm{N},H^1}(p'_{ps}, p'_{dg})/\|p'_{dg}\|_{\mathrm{N},H^1}$
0.1	1.05×10^{-4}	5.88×10^{-5}	1.05×10^{-4}
0.5	1.03×10^{-4}	8.28×10^{-5}	2.31×10^{-4}
1.0	2.25×10^{-4}	9.87×10^{-5}	2.17×10^{-4}
1.5	2.29×10^{-4}	1.12×10^{-4}	2.74×10^{-4}
3.8	2.44×10^{-4}	1.28×10^{-4}	3.00×10^{-4}

grid, at each intermediate stage of every time instant calculation. The only method, among all the other schemes employed in this comparison, which involves similar calculations, is the modified Newmark time integrator. In this occasion though, the evaluations of the second-order spatial derivatives are performed only once in each temporal cycle, in contradiction to the case of the Runge–Kutta–Nyström method, where such computations must be carried out several times due to the intermediate stage structure of the time integration algorithm. These operations can be quite expensive whenever mixed partial derivatives appear in the formulation of the problem, and especially if curvilinear elements are involved in the subdomain topology, because of the coordinate transformations that need to be utilized. This inefficiency with the explicit discretization can possibly be overcome, if the original second-order wave evolution equation is reformulated into a first-order hyperbolic system of partial differential equations and a standard Runge–Kutta method is used for the temporal approximation. Returning to the results displayed in Table 20, we see that the implicit methods were proven to be the most efficient with respect to the CPU usage, but unfortunately occupied far more memory than all the other schemes. This is absolutely expected, since the implicit methods employ the LU-factorization algorithm for the solution inside the curvilinear elements, as well as for the confrontation of the interface problems which stem from the time integration procedure.

This numerical example enabled us to test our methodology in the framework of axisymmetric simulations over curvilinear spatial domains. The methods faced no difficulty either by the axis singularity of the wave spatial differential operator, or by the incorporation of Robin boundary conditions. Finally, let us conclude our discussion by mentioning the excellent agreement between the results provided by the weak pseudospectral approximation and those obtained by the spectral collocation form of the discontinuous Galerkin finite element method for the solution of aeroacoustic wave propagation problems.

6. Conclusions

In this paper, we have presented a weak Legendre collocation domain decomposition method for the spatial approximation of hyperbolic initial boundary value problems of second order in space and time, with mixed boundary conditions, on unstructured quadrilateral subdomain topologies. The spectral discretization method is combined with implicit and high order explicit numerical algorithms for the time integration of the resulting system of ordinary differential equations. The implicit approximation belongs to the Newmark family of time integrators and leads to a sequence of discretized elliptic problems to be solved during the temporal integration procedure. A suitable weak formulation of the influence matrix method is employed for the solution of the discrete elliptic kernels, along with a combination of direct methods for the treatment of the linear algebraic systems that arise after the full discretization. A numerical technique for avoiding the amplification of roundoff errors is also investigated. Moreover, we have studied the collaboration of the weak pseudospectral method with a high order explicit Runge–Kutta–Nyström temporal approximation method and furnished an innovative method for the treatment of boundary conditions at the intermediate stages of the time integration algorithm so as to surpass the order reduction phenomenon.
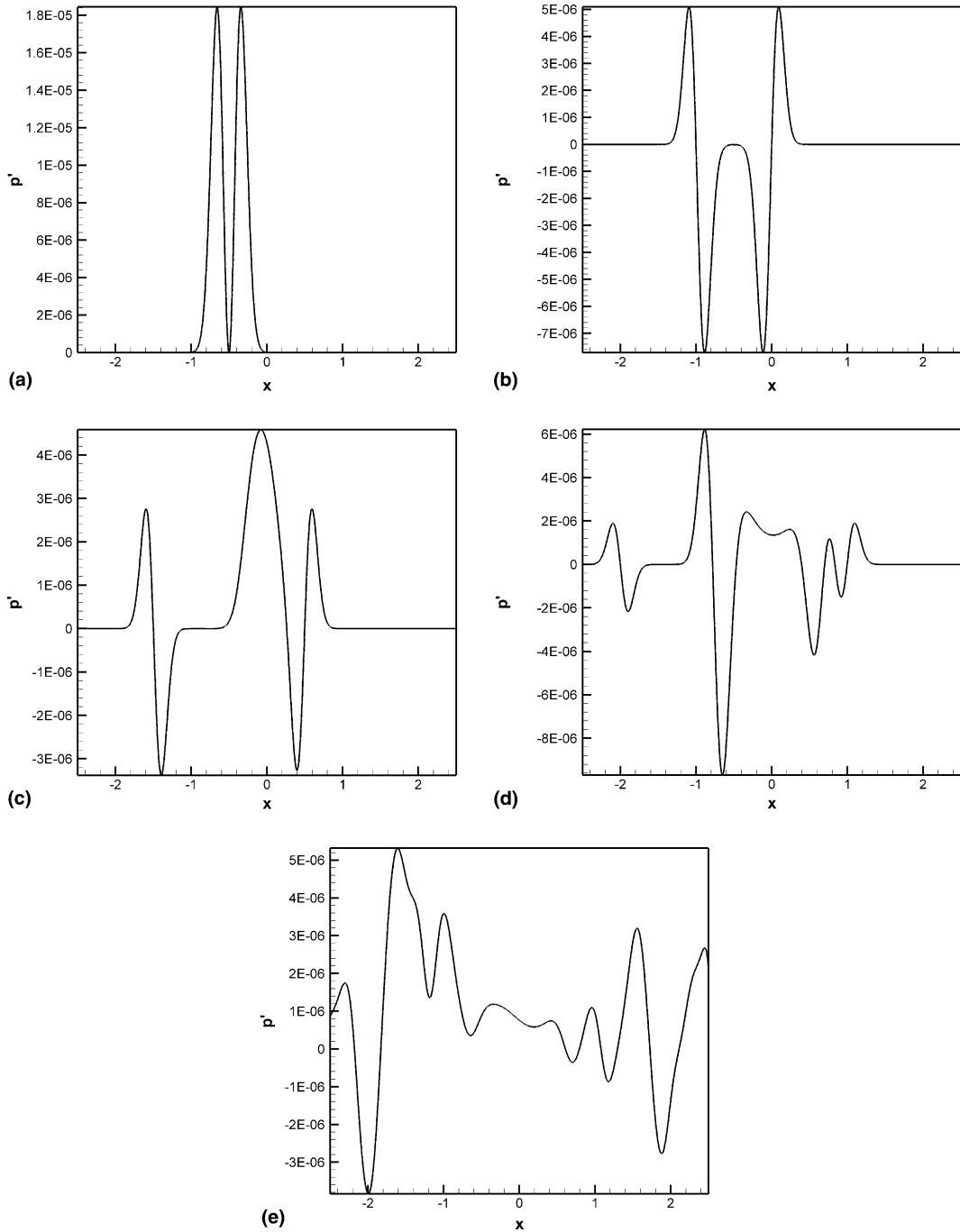
Fig. 19. Axial distribution of the pressure perturbation variable for the axisymmetric constricted tube simulation at (a) $t = 0.1$, (b) $t = 0.5$, (c) $t = 1.0$, (d) $t = 1.5$ and (e) $t = 3.8$. Continuous line: Runge–Kutta–Nyström Legendre pseudospectral solution. Dashed line: Runge–Kutta discontinuous Galerkin solution.

Table 19
Relative differences of the pressure perturbation variable as calculated by the Newmark Legendre pseudospectral and the Runge–Kutta discontinuous Galerkin methods for the acoustic pulse evolution inside an axisymmetric constricted tube

t	$d_{N,L^\infty}(p'_{ps}, p'_{dg})/\|p'_{dg}\|_{N,L^\infty}$	$d_{N,L^2}(p'_{ps}, p'_{dg})/\|p'_{dg}\|_{N,L^2}$	$d_{N,H^1}(p'_{ps}, p'_{dg})/\|p'_{dg}\|_{N,H^1}$
0.1	1.09×10^{-4}	6.14×10^{-5}	1.08×10^{-4}
0.5	1.08×10^{-4}	8.78×10^{-5}	2.29×10^{-4}
1.0	2.26×10^{-4}	1.10×10^{-4}	2.32×10^{-4}
1.5	2.43×10^{-4}	1.29×10^{-4}	2.93×10^{-4}
3.8	3.17×10^{-4}	1.58×10^{-4}	3.34×10^{-4}

Table 20
Computer code performance results for the axisymmetric acoustic pulse evolution problem

N	Me	$\Lambda_{RKDG,t}^{Me}$	$\Lambda_{RKDG,m}^{Me}$
22	RKN	1.50	0.95
	N	0.38	4.17
	MN	0.75	4.24
25	RKN	1.61	0.94
	N	0.39	5.50
	MN	0.79	5.57

Modifications appropriate for each temporal discretization method, are also formulated for dealing with the apparent singularity problem encountered by the weak formulation at axisymmetric simulations. Several examples have been included to present the performance of the various methodologies and study their capabilities for solving general hyperbolic differential equations with mixed boundary conditions over curvilinear geometries and subdomain partitions. The theoretically predicted convergence rates have been verified for all the test cases for which exact solutions were known. Finally, for the most complicated numerical experiments, our results were proven to be conformable to qualitative predictions and in very good agreement with another well-established numerical method, indicating the robustness and efficiency of the proposed algorithms.

The present spatial approximation method was designed in order to surmount some of the problems encountered by the strong collocation formulation and extend its applicability in curvilinear geometries and unstructured subdomain configurations. We proposed a unified form of the weak collocation method able of imposing boundary operators on curvilinear borders with enhanced accuracy, as well as of treating, in a natural way, the equations that govern the interface unknowns, for the solution of generic evolution equations. This method is based on a modified variational formulation of the continuous problem and manages to deliver geometrically convergent phase and dissipation errors with negligible reflections at the interface points between adjacent elements, a fact rather crucial for the study of wave propagation phenomena. Furthermore, the spatial discretization algorithm did not face any difficulty in approximating problems over curvilinear geometries and unstructured subdomain partitions, since its properties remained unaffected by the underintegration performed because of the replacement of the integral forms with discrete inner products in the presence of coordinate transformations and variable metric factors. The proposed combination of the pseudospectral method with two representative members from the families of implicit and explicit temporal approximation methods, was found to be very computationally efficient and thus enabling the successful utilization of the overall methodology for the study of various wave evolution problems.

Acknowledgement

References

[1] D. Gottlieb, S.A. Orszag, Numerical Analysis of Spectral Methods: Theory and Applications, Society for Industrial and Applied Mathematics, Philadelphia, PA, 1977.

[2] C. Canuto, M.Y. Hussaini, A. Quarteroni, T.A. Zang, Spectral Methods in Fluid Dynamics, Springer, New York, 1987.

[3] J.P. Boyd, Chebyshev and Fourier Spectral Methods, Dover, New York, 2001.

[4] D. Funaro, A variational formulation for the Chebyshev pseudospectral approximation of Neumann problems, SIAM J. Numer. Anal. 27 (1990) 695.

[5] C. Carlenzoli, P. Gervasio, Effective numerical algorithms for the solution of algebraic systems arising in spectral methods, Appl. Numer. Math. 10 (1992) 87.

[6] F. Maggio, A. Quarteroni, Acoustic wave simulation by spectral methods, East-West J. Numer. Math. 2 (1994) 129.

[7] E. Faccioli, F. Maggio, A. Quarteroni, A. Tagliani, Spectral-domain decomposition methods for the solution of acoustic and elastic wave equations, Geophysics 61 (1996) 1160.

[8] E. Faccioli, F. Maggio, R. Paolucci, A. Quarteroni, 2D and 3D elastic wave propagation by a pseudo-spectral domain decomposition method, J. Seism. 1 (1997) 237.

[9] D. Kondaxakis, S. Tsangaris, A weak Legendre collocation spectral method for the solution of the incompressible Navier–Stokes equations in unstructured quadrilateral subdomains, J. Comput. Phys. 192 (2003) 124.

[10] R. Dautray, J.-L. Lions, Mathematical Analysis and Numerical Methods for Science and TechnologyEvolution Problems I, vol. 5, Springer, Berlin, 1987.

[11] J.P. Boyd, N. Flyer, Compatibillity conditions for time-dependent partial differential equations and the rate of convergence of Chebyshev and Fourier spectral methods, Comput. Meth. Appl. Mech. Eng. 175 (1999) 281.

[12] E. Zampieri, A. Tagliani, Numerical approximation of elastic waves equations by implicit spectral methods, Comput. Meth. Appl. Mech. Eng. 144 (1997) 33.

[13] A. Quarteroni, A. Tagliani, E. Zampieri, Generalized Galerkin approximations of elastic waves with absorbing boundary conditions, Comput. Meth. Appl. Mech. Eng. 163 (1998) 323.

[14] D.A. Kopriva, J.H. Kolias, A conservative staggered-grid Chebyshev multidomain method for compressible flows, J. Comput. Phys. 125 (1996) 244.

[15] D. Givoli, I. Patlashenko, Finite-element solution of nonlinear time-dependent exterior wave problems, J. Comput. Phys. 143 (1998) 241.

[16] P.A. Raviart, J.M. Thomas, Introduction à l'analyse numérique des équations aux dérivées partielles, Masson, Paris, 1983.

[17] D. Pathria, The correct formulation of intermediate boundary conditions for Runge–Kutta time integration of initial boundary value problems, SIAM J. Sci. Comput. 18 (1997) 1255.

[18] M.P. Calvo, C. Palencia, Avoiding the order reduction of Runge–Kutta methods for linear initial boundary value problems, Math. Comp. 71 (2001) 1529.

[19] M. Abramowitz, I.A. Stegun (Eds.), Handbook of Mathematical Functions, Dover, New York, 1972.

[20] E. Serre, J.P. Pulicani, A three-dimensional pseudospectral method for rotating flows in a cylinder, Comput. Fluids 30 (2001) 491.

[21] W. Huang, D.M. Sloan, Pole condition for singular problems: the pseudospectral approximation, J. Comput. Phys. 107 (1993) 254.

[22] R. Verzicco, P. Orlandi, A finite-difference scheme for three-dimensional incompressible flows in cylindrical coordinates, J. Comput. Phys. 123 (1996) 402.

[23] K. Mohseni, T. Colonius, Numerical treatment of polar coordinate singularities, J. Comput Phys. 157 (2000) 787.

[24] G.S. Constantinescu, S.K. Lele, A highly accurate technique for the treatment of flow equations at the polar axis in cylindrical coordinates using series expansions, J. Comput. Phys. 183 (2002) 165.

[25] V.S. Ryaben'kii, S.V. Tsynkov, V.I. Turchaninov, Global discrete artificial boundary conditions for time-dependent wave propagation, J. Comput. Phys. 174 (2001) 712.

[26] F.Q. Hu, M.Y. Hussaini, J.L. Manthey, Low-dissipation and low-dispersion Runge–Kutta schemes for computational acoustics, J. Comput. Phys. 124 (1996) 177.

[27] C.A. Kennedy, M.H. Carpenter, R.M. Lewis, Low-storage, explicit Runge–Kutta schemes for the compressible Navier-Stokes equations, Appl. Numer. Math. 35 (2000) 177.

[28] R. Renaut, J. Fröhlich, A pseudospectral Chebyshev method for the 2D wave equation with domain stretching and absorbing boundary conditions, J. Comput. Phys. 124 (1996) 324.

[29] B. Engquist, A. Majda, Absorbing boundary conditions for the numerical simulation of waves, Math. Comp. 31 (1977) 629.
[30] B. Engquist, A. Majda, Radiation boundary conditions for acoustic and elastic wave calculations, Commun. Pure Appl. Math. 32 (1979) 313.
[31] A. Bayliss, E. Turkel, Radiation boundary conditions for wave-like equations, Commun. Pure Appl. Math. 33 (1980) 707.
[32] X. Antoine, H. Barucq, Bayliss-Turkel-like radiation conditions on surfaces of arbitrary shape, J. Math. Anal. Appl. 229 (1999) 184.
[33] D. Givoli, High-order local non-reflecting boundary conditions: a review, Wave Motion 39 (2004) 319.
[34] R. Kosloff, D. Kosloff, Absorbing boundaries for wave propagation problems, J. Comput. Phys. 63 (1986) 363.
[35] M. Israeli, S.A. Orszag, Approximation of radiation boundary conditions, J. Comput. Phys. 41 (1981) 115.
[36] F. Bassi, S. Rebay, High-order accurate discontinuous finite element solution of the 2D Euler equations, J. Comput. Phys. 138 (1997) 251.
[37] B. Cockburn, C.-W. Shu, The Runge–Kutta discontinuous Galerkin method for conservation laws V, J. Comput. Phys. 141 (1998) 99.
[38] D.A. Kopriva, S.L. Woodruff, M.Y. Hussaini, Discontinuous spectral element approximation of Maxwell's Equations, in: B. Cockburn, G. Karniadakis, C.-W. Shu (Eds.), Discontinuous Galerkin Methods, Lecture Notes in Computational Science and Engineering, vol. 11, Springer, Berlin, 2001, p. 355.
[39] D.A. Kopriva, S.L. Woodruff, M.Y. Hussaini, Computation of electromagnetic scattering with a non-conforming discontinuous spectral element method, Int. J. Num. Meth. Eng. 53 (2002) 105.
[40] M. Sussman, M.Y. Hussaini, A discontinuous spectral element method for the level set equation, J. Sci. Comp. 19 (2003) 479.
[41] F.Q. Hu, M.Y. Hussaini, P. Rasetarinera, An analysis of the discontinuous Galerkin method for wave propagation problems, J. Comput. Phys. 151 (1999) 921.
[42] D. Stanescu, D.A. Kopriva, M.Y. Hussaini, Dispersion analysis for discontinuous spectral element methods, J. Sci. Comp. 15 (2000) 149.
[43] D. Stanescu, M.Y. Hussaini, F. Farassat, Aircraft engine noise scattering by fuselage and wings: a computational approach, J. Sound Vib. 263 (2003) 319.
[44] P.L. Roe, Approximate Riemann Solvers, parameter vectors, and difference schemes, J. Comput. Phys. 43 (1981) 357.